UNIVERSITÀ DEGLI STUDI DI PADOVA

Dipartimento di Fisica e Astronomia "Galileo Galilei"

Master Degree in Astrophysics & Cosmology

Final Dissertation

Investigating the role of opacity in reconciling the Standard Solar Model and Helioseismology

Thesis supervisor

Prof.ssa Paola Marigo

Thesis co-supervisors

Prof. Alessandro Bressan

Dr. Guglielmo Volpato

Candidate

Daniele Mantovani

Academic Year 2022/2023

To my family,
for always being there.

To my high school math teacher,
for always encouraging me to give my best
and to follow my passions.

Contents

Introduction

Over the last 20 years, advances in determining the chemical composition of the Sun have adversely affected the agreement between Standard Solar Models (SSMs) and helioseismology, to the point where SSMs can no longer be made to agree with helioseismic constraints. Agreement with helioseismology could be restored by either increasing atomic opacity at the bottom of the convection zone and decreasing it towards the solar center by 30%, or by returning to older, higher metal abundances. Recently Bailey et al. (2015) has showed how Fe opacity could be underestimated by some 60% for conditions close to those of the bottom of the solar convective envelope, and how increasing its value alone could resolve about half the discrepancy between SSMs and helioseismology.
Even more recently Magg et al. (2022) have published a new high-Z solar chemical composition obtained considering new oscillator strengths for atomic calculations, which gives a value of $(Z/X)_{\odot} = 0.0225$, close to the old 0.0230 of Grevesse and Sauval (1998). Magg et al. claim that SSMs realized with this new composition are consistent with the solar structure obtained from helioseismic observations, ruling out the need of an increase of atomic opacities. The goal of this work is to investigate the effect of increasing the Fe opacity on SSMs assuming Magg et al. (2022) chemical composition, calibrating models computed with different opacity tables from the OPAL and TOPS projects and trying to give an estimate for the Fe opacity values that best reproduce the helioseismic constraints. A correction factor is applied to Fe monochromatic opacity prior to the computation of the Rosseland mean opacity, and an MCMC technique is used to calibrate SSMs and obtain the models that best reproduce the solar data.
This work is organized as follows. Chapter 1 provides a brief description of the Sun, defining SSMs and their characteristics, and providing a short overview of helioseismology and how it relates to solar structure. Chapter 2 presents the technique I used to realize and calibrate the models and the results of this calibration, including the effects of increasing Fe opacity and introducing non-zero envelope overshooting in modeling the Sun. Chapter 3 shows how well the considered models behave in reproducing the measured solar neutrino flux, including considerations for the effects of the reaction rates used in neutrino-producing reactions. Finally, Chapter 4 concludes the analysis, presenting the models that best describe solar data.

Chapter 1

Standard Solar Models

The Sun is our closest star. This means its properties are easier to observe and determine than those of farther stars, making it the ideal candidate for testing stellar models. Standard Solar Models (SSMs) represent a simplified physical description of the Sun; in their framework one can draw predictions on the properties of the Sun, which are to be tested against observations. Despite the many approximations SSMs use, they provide a quite successful description of many properties of the Sun, allowing to get information both about its photospheric properties and its internal structure. The solar interior can also be investigated by studying the frequency and oscillations of acoustic waves reverberating through it; this goes under the name of helioseismology. Until recent years SSMs predictions and the properties inferred by helioseismology have shown excellent agreement, confirming the validity of the SSM. However, in the last twenty years the concordance between SSMs and helioseismology was altered by new determinations of solar photospheric abundances by Asplund et al. (2005) using new time-dependent 3D radiation hydrodynamic (3D-RHD) models for stellar atmospheres. These newly determined abundances are lower than the previously commonly adopted Grevesse and Sauval (1998) abundances. Adopting these new abundances in SSMs led to loose the previous agreement with helioseismic data. The discrepancy between helioseismic results and SSMs is often called the solar abundance problem and is still an open problem of modern astrophysics. Although yet unresolved, the solar abundance problem has motivated further investigation on the physical inputs of solar models, in particular on the improvement of nuclear reaction rates, on theoretical and experimental determination of radiative opacities and on the appropriate equation of state to describe solar interiors.

1.1 Overall properties of the Sun

Many of the properties of the Sun are known with high precision thanks to observations, without the need of modeling its structure.
The age of the Sun $t_\odot$ can be determined by studying the age of meteorites, together with models for the formation and the evolution of the solar system. Guenther (1989) determined an age of $t_\odot = (4.49 \pm 0.04) \times 10^9$ yr. Guenther also showed that, although the commonly used solar age for SSMs at that time was 4.7×10^9 yr, the calibrated parameters of the model were not significantly modified by that small age difference. The value proposed by Guenther was later revised to $t_\odot = (4.566 \pm 0.005) \times 10^9$ yr (Bahcall

et al., 1995, appendix). Stellar evolution models suggest that the Sun is now halfway through its life, and will remain in the main sequence for roughly another 4.5×10^9 yr.
The mass of the sun $M_\odot$ can be determined thanks to the study of planetary motion: the product $GM_\odot$ can be calculated from Kepler's third law, so that the accuracy limit for $M_\odot$ is set by how precisely the gravitational constant G is known. The nowadays commonly used value is $M_\odot = 1.989 \times 10^{33}$ g. We know the mass of the Sun varies during its life because of mass loss through stellar winds; the estimated mass loss rate is roughly $\dot{M}_\odot \simeq 10^{-14}\,\mathrm{M}_\odot/\mathrm{yr}$, with no significant change during the main sequence, so the solar mass can be taken as approximately constant, at least during the main sequence.
The solar radius $R_\odot$ can be determined from the apparent diameter of the Sun knowing Sun-Earth distance, or by transit and eclipse measurements. Recent solar models have used $R_\odot = 6.9598 \times 10^{10}$ cm (Guenther et al., 1992).
The solar luminosity $L_\odot$ is determined from solar radiance measurements by satellites (e.g. Willson and Hudson, 1991). The usually adopted value is $L_\odot = 3.846 \times 10^{33}$ erg/s (Guenther et al., 1992).
From the determination of the luminosity and the radius of the Sun one can easily evaluate its effective temperature $T_{\mathrm{eff},\odot}$, which is the temperature of a black body radiating the same energy flux at the surface of the star, and is a good measure of the temperature of the photosphere. It follows that the luminosity, the radius and the effective temperature are linked by Stefan-Boltzmann law,

$$L = 4\pi R^2 \sigma T_{\mathrm{eff}}^4, \tag{1.1}$$

σ being Stefan-Boltzmann constant. With the values previously stated for the luminosity and the radius, the effective temperature of the Sun is $T_{\mathrm{eff},\odot} = 5778$ K.

1.2 Solar chemical composition

Determining the chemical abundance of elements in the Sun usually requires a spectroscopic analysis of the solar photosphere. Such a determination needs to be coupled with detailed models of the solar photosphere and with radiative transfer calculations, in order to link chemical abundances to the intensity and the shape of lines and to the position where they form in the photosphere. The introduction of 3D-RHD models for the photosphere and of non-local thermodynamic equilibrium calculations for line formation led to a revision downward for many abundances. A detailed review of the most used chemical compositions and their relation with the solar abundance problem can be found in Serenelli (2016). Table 1.1 shows the photospheric abundances determined by different authors through the years: Grevesse and Sauval (1998, hereafter GS98), Asplund et al. (2009, hereafter AGSS09), Caffau et al. (2011, hereafter C11), Asplund et al. (2021, hereafter AAG21) and Magg et al. (2022, hereafter MBSS22). The last row of the table shows the photospheric hydrogen-to-metal ratio $(Z/X)_\odot$ at the present day for each chemical composition. AGSS09 is a revision of the abundances given by Asplund et al. (2005) a few years before. Photospheric abundances are given in the so-called astronomical scale, i.e. normalized to the hydrogen number density as

$$A(El.) = \log \epsilon(El.) = \log \frac{n(El.)}{n(\mathrm{H})} + 12, \tag{1.2}$$

Table 1.1. Solar photospheric composition for different authors for most relevant metals. Abundances given in the astronomical scale $A(El.) = \log[n(El.)/n(\mathrm{H})] + 12$ as discussed in the text.

Element	GS98	AGSS09	C11	AAG21	MBS22
C	8.52	8.43	8.50	8.46	8.56
N	7.92	7.83	7.86	7.83	7.98
O	8.83	8.69	8.76	8.69	8.77
Ne	8.08	7.93	8.05	8.06	8.15
Mg	7.58	7.60	7.54	7.55	7.55
Si	7.55	7.51	7.52	7.51	7.59
S	7.33	7.13	7.16	7.12	7.16
Fe	7.50	7.50	7.52	7.46	7.50
$(Z/X)_\odot$	0.0230	0.0180	0.0209	0.0187	0.0225

where $\log n(\mathrm{H}) = 12$. GS98 represents the old high-Z chemical composition, while the introduction of 3D-RHD models led to lower metal abundances, like those of AGSS09 and C11, hence the name of low-Z chemical composition. AGSS09 is one of the most used chemical compositions for the Sun. It has abundances $> 30\%$ lower than those of GS98. C11 has CNO abundances which are intermediate between those of GS98 and AGSS09, obtained via 3D-RHD independent models. The latest revision of spectroscopic results AAG21 shows results similar to AGSS09. MBS22 is a new solar composition obtained combining new up-to-date solar observational data, non-local thermodynamic equilibrium modeling, different atmospheric models and new oscillator strengths for atomic transitions. Interestingly the calculations predict a value of $(Z/X)_\odot$ which is higher than previous models (26% higher than AGSS09, 10% higher than C11), comparable with the old value obtained by GS98 (1% difference). However, this agreement is just a numerical coincidence since the internal distribution of metals is different. For example, MBS22 O abundance is 15% lower than GS98, while Si abundance is 10% higher.

Along with photospheric determinations, many refractory elements can be precisely determined from chondritic CI meteorites, which are representative of the average cosmic matter the solar system formed from (see Lodders et al., 2009). Refractory elements constitute up to 20% of the total metal abundance in stars and are particularly important for their contribution to the radiative opacity in solar interiors. Meteoritic abundances have remained robust through the years, while the spectroscopic ones slowly evolved towards the meteoritic values. This seems to suggest that meteoritic determinations are more accurate, and indeed usually one combines meteoritic abundances for refractories and photospheric abundances for volatile elements in building SSMs.

Meteoritic abundances are usually given in the so-called cosmochemical scale, meaning they are normalized to the Si number density. Matching the cosmochemical scale and the astronomical scale then requires an anchor point between the two. This is usually done by setting the Si abundance to be equal on both scales. So meteoritic abundances in the astronomical scale can be found as

$$A(El.) = c + \log n(El.), \tag{1.3}$$

where c is a constant to be found imposing the value for $A(\mathrm{Si})$ to match the photospheric value, with $n(\mathrm{Si}) = 10^6$.
Uncertainties on photospheric abundances are difficult to quantify, since they depend on the details of the atmospheric models involved and on the selection of spectral lines, and are thus to be taken as indicative. On the other hand uncertainties on meteoritic abundances are smaller and much less prone to systematic errors, since no modeling is involved in this case. This again reinforces the idea that meteoritic abundances should be used in constructing solar models, when available.

1.3 Solar structure and evolution

Before describing the physics involved in SSMs, it is useful to remember that they are built on some key assumptions.

- The Sun is considered to be isolated in space, so that its evolution is fully determined by its intrinsic properties, such as the mass and the initial composition.
- The model is considered to be spherically symmetric. Spherical symmetry is prompted by self-gravity and is usually a good approximation, but deviations may arise because of non-central forces, like those originating from rotation and magnetic fields. The Sun is known to exhibit many features due to magnetic fields (see Schrijver and Zwaan, 2000), but the field strength is negligible when compared to gravity. Rotation can be more important, in particular because it also induces rotational mixing, and there is a lot of evidence about the rotation of the Sun (e.g. Beck, 2000). However, for the Sun rotational forces are again small compared to gravity.
- The Sun is assumed to have formed with homogeneous chemical composition, a reasonable assumption since the molecular clouds out of which stars form are well-mixed.

Once these assumptions are made, a SSM is a solution of the basic equations of stellar structure, which are

$$\frac{\partial r}{\partial m} = \frac{1}{4\pi r^2 \rho}, \tag{1.4}$$

$$\frac{\partial P}{\partial m} = -\frac{Gm}{4\pi r^4}, \tag{1.5}$$

$$\frac{\partial l}{\partial m} = \epsilon_{\mathrm{nuc}} - \epsilon_\nu - T\frac{\partial s}{\partial t}, \tag{1.6}$$

$$\frac{\partial T}{\partial m} = -\frac{Gm}{4\pi r^4}\frac{T}{P}\nabla. \tag{1.7}$$

Here r is the radial distance from the center, m is the mass enclosed by a sphere of radius r, ρ is the density, P is the pressure, T is the temperature, l is the local luminosity (i.e. the energy per unit time emitted by a sphere of radius r), ϵ_{nuc} is the energy per unit time generated by nuclear reactions, ϵ_ν is the energy per unit time lost because of neutrinos, s is the specific entropy (i.e. the entropy per unit mass) and $\nabla = \mathrm{d}\ln T/\mathrm{d}\ln P$ is the temperature gradient.

Equation (1.4) represents mass conservation, and establishes the equivalence between Eulerian coordinates, with the distance from the center expressed as r, and Lagrangian coordinates, with the distance from the center characterized by $m(r) = \int_0^r 4\pi r^2 \rho \, \mathrm{d}r$.
Equation (1.5) is the hydrostatic equilibrium equation, representing the balance between gravitational forces and pressure forces.
Equation (1.6) is instead an energy balance equation: the nuclear energy rate equilibrates the energy loss from a sphere of mass m, once neutrino losses are subtracted from this energy. The specific entropy term takes into account quasi-static gravitational readjustments due to heat transfer.
Equation (1.7) describes the transfer of energy from the center to the surface. The temperature gradient ∇ depends on the physical mechanism responsible for energy transport being radiation, in which case the radiative temperature gradient ∇_{rad} is used, or convection, in which case the real temperature gradient ∇ is used. When radiative transfer is the main energy transport mechanism the temperature gradient sollows the radiative one, which is given by

$$\nabla_{\mathrm{rad}} = \frac{3}{16\pi acG} \frac{\kappa P}{T^4} \frac{l}{m}, \tag{1.8}$$

where a is the radiation density constant, c is the speed of light and κ is the opacity, a key parameter describing the interaction of light with matter defined so that the mean free path of photons is $\ell_{\mathrm{ph}} = 1/\kappa\rho$. The opacity has different contributions from the different physical processes via which radiation interacts with matter (see Section 1.3.1). On the other hand when convection is the main mechanism responsible for energy transfer one needs to specify a prescription for the description of convective transfer. The onset of convection as the main energy transfer mechanism instead of radiative diffusion is usually given by Schwarzschild criterion: regions where $\nabla_{\mathrm{rad}} < \nabla_{\mathrm{ad}}$, with $\nabla_{\mathrm{ad}} = (\partial \ln T / \partial \ln P)_s$ is the adiabatic temperature gradient, the derivative taken at constant entropy, are stable against convection. When $\nabla_{\mathrm{rad}} > \nabla_{\mathrm{ad}}$ convection sets on, becoming more efficient than radiative diffusion in transporting energy. In this case it is fundamental to describe the temperature gradient ∇, and in particular the so-called superadiabaticity $\nabla - \nabla_{\mathrm{ad}}$, giving the deviations of the temperature gradient from the adiabatic one. The condition $\nabla_{\mathrm{rad}} > \nabla_{\mathrm{ad}}$ can be satisfied in regions where a large energy flux l/m is produced, like in the center of massive stars, or in regions where the opacity κ is high and the temperature T is low, like in the outer regions close to the surface. This is the case for the Sun, which has a convective layer extending from its surface up to a radial coordinate of $0.713\,\mathrm{R}_\odot$ (Basu and Antia, 1997).
Equations (1.4) to (1.7) determine the structure of the model, while the time evolution is governed by a fifth equation for the chemical composition, which is

$$\frac{\partial X_i}{\partial t} = \frac{A_i m_u}{\rho} \left[-\sum_j (1 + \delta_{ij}) r_{ij} + \sum_k \sum_l r_{kl,i} \right] + \text{mixing terms}. \tag{1.9}$$

Here X_i is the mass fraction of the i-th species, A_i its atomic mass, m_u is the atomic mass unit and r_{ij} and $r : kl, i$ are nuclear reaction rates. The first term in square brackets takes into account all the reactions depleting the species i as $i + j \rightarrow$ products, while the second one is the sum over all the reactions producing the species i as $k + l \rightarrow i +$ other products. This equation can be complicated by the mixing term, which takes into

account other mixing processes such as turbulence, diffusion and settling (see Proffitt and Michaud, 1991).
The five equations are non-linear and coupled, so they must be solved together using using numerical procedures. The SSM is the solution of these equations at the present day age of the Sun $t_\odot$. Such a solution depends on the initial conditions of the model, in particular on the initial composition, usually described via $Z_{\rm ini}$ and $Y_{\rm ini}$, and from $X_{\rm ini} + Y_{\rm ini} + Z_{\rm ini} = 1$ the composition is fully determined. The standard procedure to obtain a SSM is to treat $Y_{\rm ini}$ and $Z_{\rm ini}$ as free parameters of the model together with the mixing length parameter α used to describe convection (see Section 1.3.2), and calibrate the model to reproduce the solar luminosity $L_\odot$, effective temperature $T_{\rm eff,\odot}$ and surface composition at the present day age of the Sun $t_\odot$. Roughly speaking α is related to $T_{\rm eff,\odot}$, $Y_{\rm ini}$ to $L_\odot$ and $Y_\odot$ and $Z_{\rm ini}$ to $(Z/X)_\odot$, although the three adjustable parameters depend on all the observational constraints and are thus correlated.
In order to solve eqs. (1.4) to (1.7) and (1.9) one needs to specify the underlying physics giving prescriptions for the quantities appearing on the right-hand sides as functions of P, T and the composition X_i. The main input physics needed to solve the equations is discussed below.

1.3.1 Equation of state and opacity

Equations (1.4) and (1.5) can be solved when coupled with an Equation of State (EoS) describing the pressure P as a function of the density ρ, the temperature T and the chemical composition X_i. The computation of the EoS requires to describe the state of all the main particle species (atoms, ions, molecules, electrons, etc.), following their abundance and evolution. The different particle species have also impact on the calculation of the radiative opacity κ, which depends on the population of all electron energy levels that contribute significantly to photoabsorption and photon scattering in the material, and is then directly linked to the EoS.
There are two different formulations commonly used for the EoS: the first one is the so-called physical picture, which treats all the different particles such as electrons and nuclei as distinct, and looks at the electric interaction between them. In this way environmental effects are included naturally, since the interactions lead to the formation of clusters of particles representing ions, atoms and molecules interacting with the environment. The most used description of the EoS in the physical picture is that of the OPAL project (Iglesias and Rogers, 1996).
The other possibility is the chemical picture, which considers atoms, ions and molecules as given, and looks at the reactions between them, like the ionization of atoms, or the dissociation of a molecule. Environmental effects in this picture are treated as perturbations. Examples of chemical picture EoS are the MHD multi-species EoS used by the OP project (Hummer and Mihalas, 1988) and the CHEMEOS used in the ATOMIC opacity code (Colgan et al., 2016) in Los Alamos TOPS project.
In order to calculate opacity tables with either picture, one has to take into account nuclear processes, the computation of which requires the knowledge of nuclear cross sections. Determining these cross sections can be challenging because of the reaction energies relevant for stellar interiors. The most used collection of reaction parameters is that of the JINA REACLIB database (Cyburt et al., 2010).

1.3.2 Convection

In the Sun convection occurs in the outer 29% of the solar radius, as determined with helioseismologic studies by Basu and Antia (1997). In this region it is necessary to describe the temperature gradient ∇, and in particular the superadiabaticity $\nabla - \nabla_{\rm ad}$. The reference theory for the description of convection in stellar interiors is the Mixing Length Theory (MLT), originally proposed by Böhm-Vitense (1958). The main idea of the MLT is to describe the bulk motions of fluids in analogy with molecular heat transfer. It considers "particles" of fluid with local uniform physical characteristics and traces their movement. A particle will be in pressure equilibrium with its surroundings, but not in thermal equilibrium, so hot particles will move toward cooler regions, while cooler particles will move toward cooler regions. As hot particles rise they expand and lose their homogeneous physical characteristics, and the same happens to cool particles, which sink and compress. The typical distance such a particle can travel before losing its properties is called the mixing length α, which can be thought of as the mean free path of the particle. The overall movement of these particles leads to a net outward flux of energy, a simple toy model of which is

$$F_{\rm conv} = \frac{1}{2}\rho v c_P T \frac{\lambda}{H_P}(\nabla - \nabla_{\rm ad}), \tag{1.10}$$

with ρ the density, v the velocity, c_P the specific heat and $\alpha = \lambda / H_P$ the mixing length given as a fraction of the pressure scale height $H_P = |{\rm d}r/{\rm d}\ln P|$, the distance over which the pressure changes by an e-folding factor. The flux $F_{\rm conv}$ is determined by the superadiabaticity $\nabla - \nabla_{\rm ad}$ and the mixing length α, which modulates the efficiency of convective energy transport: the larger α, the larger the energy flux transported by convection. Moreover, convection results in bulk motions of matter, favoring chemical mixing. In solar models α is left as a free parameter and it is determined by calibrating the model to reproduce the known properties of the Sun. A nice review of the MLT and its applications in stellar models, including some possible alternatives and extensions, can be found in Joyce and Tayar (2023).

The boundary of convective regions is usually given by Schwarzschild criterion on the basis of the local temperature gradient. However when convective bubbles reach this point their acceleration vanishes, but their velocity is still non-zero. This means convective bubbles can penetrate beyond the boundary of the convective region up to some point where their velocity vanishes and they dissolve, and this point should be taken as the true boundary. This phenomenon is called convective overshooting. The appropriate treatment of overshooting usually involves non-local MLTs (Shaviv and Salpeter, 1973; Bressan et al., 1981, 2012). The main idea is to follow the whole motion of a convective bubble from its formation to its dissolution, solving its equation of motion and determining the true extent of the convective zone.

Overshooting in the Sun can happen below the convective envelope. The main parameter describing the overshoot is the mean free path of convective bubbles *below* the convective zone, given in terms of the local pressure scale height as $\Lambda_e H_P$. The possibility of a significant overshoot region at the base of the convective envelope was initially explored by Alongi et al. (1991). Two important observational effects related to this phenomenon have been studied: the location of the RGB Bump in the red giant branch (RGB) of low-mass stars and the extension of the blue loops in intermediate mass stars. Both effects have been found to be better explained by a moderate amount

of overshoot, with a typical extension below the border of approximately $0.25 - 1.0 H_P$. However solar model calibration reproduces the transition between the fully adiabatic envelope and the underlying radiative region in the Sun without the need of overshooting. This does not exclude the possibility that convection may penetrate just below the fully adiabatic region in the form of radiative fingers, which can induce significant mixing. Recent arguments suggest that such a mechanism could better align with the physical state of matter in this transition region, as inferred from solar oscillation data (Christensen-Dalsgaard et al., 2011). The magnitude of this effect has been estimated to be around $0.4 H_P$, although it is also consistent with a larger value of $0.6 H_P$, which aligns well with the value adopted since Alongi et al. (1991).

1.3.3 Nuclear reactions

Nuclear reactions are fundamental in stellar models since they are the main source of energy in stars, and they determine the evolution of chemical abundances. Energy generation in the Sun results from the fusion of hydrogen into helium with the net reaction

$$4\,^1\mathrm{H} \longrightarrow {}^4\mathrm{He} + 2\,\mathrm{e}^+ + 2\,\nu_e. \tag{1.11}$$

The path by which this reaction takes place involves different sequences of reaction depending on the temperature at which they take place. The two main possibilities are the pp-chain and the CNO cycle. Then there are several other reactions involving heavier elements, which contribute less to the energy production but are important to follow correctly the chemical composition of the Sun during its evolution. As mentioned before, a complete collection of nuclear reaction rates can be found in the JINA REACLIB database (Cyburt et al., 2010).
Following nuclear reactions is also important to have a correct description of neutrino losses: since neutrinos do not interact with matter they can escape freely from the star, representing an energy loss. These neutrinos travel to the Earth, where the solar neutrino flux can be measured. Calibrating solar models to reproduce the correct neutrino fluxes for the different reactions, which is possible because the neutrino energy loss is different for each reaction, can help in understanding the correct processes that are going on inside the Sun and what their contribution to the total solar energy is. A summary of the state-of-art SSMs neutrino results can be found in Serenelli (2016).

1.4 Helioseismology

Solar oscillations have an important diagnostic potential. These observed oscillations exhibit very small amplitudes, so they can be described as linear perturbations around the solar models generated through evolutionary calculations. Consequently, the frequencies of these oscillations serve as direct indicators of the properties of the solar interior: by utilizing a solar model, one can accurately calculate the pertinent aspects of the frequencies, and any differences between the observed and calculated frequencies can be attributed to something missing or not treated properly in the model.
The basic idea behind solar oscillations is the perturbation up to linear order of the continuity equation

$$\frac{\partial \rho}{\partial t} + \boldsymbol{\nabla} \cdot (\rho \mathbf{v}) = 0 \tag{1.12}$$

and Euler equation

$$\frac{\partial \mathbf{v}}{\partial t} + (\mathbf{v} \cdot \boldsymbol{\nabla})\mathbf{v} = -\frac{1}{\rho}\boldsymbol{\nabla} P + \mathbf{g} \tag{1.13}$$

for the fluid in stellar interiors. Here $\mathbf{g} = -\boldsymbol{\nabla}\Phi$ is the gravitational acceleration, with Φ obeying Poisson equation $\nabla^2\Phi = 4\pi G\rho$. Since in stars the average period of oscillations is much shorter than the timescale for energy exchange, one can assume the adiabatic approximation. Given a spherically symmetric and time independent equilibrium, the solutions for the perturbed equations can be separated in time, radial and angular components. The time components are simple harmonic functions $e^{-i\omega t}$ characterized by an oscillatory frequency ω, while the angular components are the spherical harmonics $Y_l^m(\theta, \phi)$. The radial components obey different perturbed equations which offer solutions only for discrete values of ω. Thus for each (l, m) there is a set of frequencies ω_{nlm}, distinguished by their radial order n. Within the adiabatic approximation these frequencies are completely determined by ρ, P, g and Γ_1 as a function of the distance r from the center. However, since we are dealing with stellar interior $\mathbf{g}$ is given by

$$\mathbf{g} = -\frac{Gm}{r^2}\hat{\mathbf{r}}, \tag{1.14}$$

and it is related to P and ρ through eqs. (1.4) and (1.5). So specifying just two of the four quantities above is sufficient to completely determine the oscillation frequencies, and vice-versa the observed frequencies solely offer direct information regarding these "mechanical" quantities. Other properties can be determined if further information is provided, such as an EoS or the other equations of stellar structure.
The observed solar oscillations are in most cases predominantly of acoustic nature (the so-called "p modes"), and frequencies are most sensitive to the sound speed, which is

$$c_s^2 = \left(\frac{\partial \ln P}{\partial \ln \rho}\right)_s = \Gamma_1 \frac{P}{\rho} \simeq \frac{\Gamma_1 k_B T}{\mu m_u}, \tag{1.15}$$

the last equality coming from the fact that solar interior can be approximated as an ideal gas with EoS $P = k_B \rho T / \mu m_u$, with k_B Boltzmann constant and μ the mean molecular weight. The approximate behavior of p modes inside the Sun is shown in Figure 1.1. As r decreases the temperature, and hence the sound speed, increases, and the increasing sound speed makes sound rays bend, until they reach an inner turning point and then proceed outwards. The modes observed as global oscillations on the stellar surface are the result of the interference between these waves. The turning point is located closer to the center for higher angular degree l and lower frequency ω. In particular modes with $l = 0$ penetrate the center, while modes with $l \geq 1000$ are trapped in a tiny shell close to the surface. Hence the oscillation frequencies of various modes serve as probes of distinct regions within the Sun, and through an inversion process they allow to determine the properties of the solar interior.
Solar oscillations exhibit diverse manifestations in the solar atmosphere. Changes in energy transport in the outer layers lead to oscillations in solar energy output, fluctuations in atmospheric temperature are reflected in the properties of solar spectral lines, while matter displacement can cause the atmosphere itself to move. Each of these effects allows the observation of oscillations, and since they all come from the same underlying modes, they yield the same frequencies of oscillation.

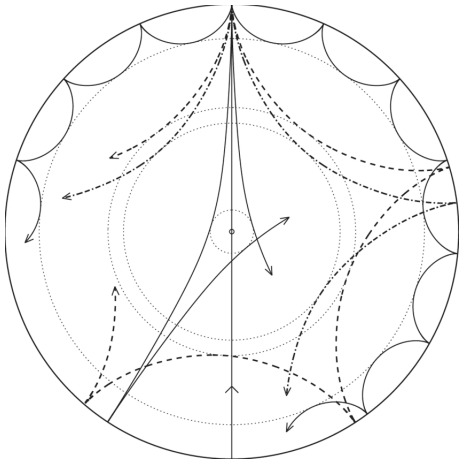

Figure 1.1. Propagation of p modes in the solar interior. Sound rays are bent by the increase in the sound speed, until they reach the inner turning point, represented by dotted lines. At the surface the waves are reflected because of the rapid decrease in density. Image from Christensen-Dalsgaard (2002).

1.4.1 Inversion for solar structure

The idea of the inversion technique is that of obtaining information on the solar interior given the differences between the observed frequencies and those predicted by the model. The starting point for inversion is the Euler equation for the perturbations, which can be rewritten as

$$\omega^2 \boldsymbol{\delta r} = \mathcal{F}(\boldsymbol{\delta r}), \tag{1.16}$$

where $\boldsymbol{\delta r}$ is the displacement of a fluid element and $\mathcal{F}$ is a linear operator. Multiplying by $\rho \boldsymbol{\delta r}^*$ and integrating over the volume the equation becomes

$$\omega^2 = \frac{\int \boldsymbol{\delta r}^* \cdot \mathcal{F}(\boldsymbol{\delta r}) \rho \, \mathrm{d}V}{\int |\boldsymbol{\delta r}|^2 \rho \, \mathrm{d}V}. \tag{1.17}$$

This equation defines a variational principle (Chandrasekhar, 1964): perturbations on the frequencies of the equilibrium model are obtained perturbing this equation. The perturbation on the right-hand side of the equation can suitably be expressed in terms of two mechanical quantities, as $\left(\rho, c_s^2\right)$. Indicating with i the couple (n, l) for simplicity, the resulting equation is

$$\frac{\delta\omega_i}{\omega_i} = \int_0^R \left[K^i_{c_s^2,\rho}(r) \frac{\delta c_s^2}{c_s^2}(r) + K^i_{\rho,c_s^2}(r) \frac{\delta\rho}{\rho}(r) \right] + I_i^{-1} F_{\mathrm{surf}}(\omega_i), \tag{1.18}$$

where $K^i_{c_s^2,\rho}$ and K^i_{ρ,c_s^2} are two functions called kernels depending on the reference model, $\delta\rho$ and δc_s^2 are the differences between the Sun and the model in the sense $\delta\rho = \rho_\odot - \rho_{\mathrm{mod}}$, $I_i = \int |\boldsymbol{\delta r}|^2 \rho \, \mathrm{d}V$ is the mode inertia and F_{surf} is a surface term coming from inadequacies in the treating of the physics of the model, which are relevant close to the surface. Inverting equation (1.18) allows to estimate $\delta c_s^2/c_s^2$ and $\delta\rho/\rho$.
The principle of the inversion technique is to use linear combinations of the above equation with different weights $d_i(r_0)$ chosen in order to obtain an average $\delta c_s^2/c_s^2$ or $\delta\rho/\rho$

near $r = r_0$ while suppressing the contributions from the other terms. For example for the sound speed one wants to get

$$\frac{\delta c_s^2}{c_s^2}(r_0) \simeq \sum_i d_i(r_0)\frac{\delta\omega_i}{\omega_i} = \int_0^R \mathcal{K}(r_0, r)\frac{\delta c_s^2}{c_s^2}(r)\,\mathrm{d}r, \tag{1.19}$$

where the last equality is valid because of equation (1.18), with the averaging kernel $\mathcal{K}(r_0, r)$ defined as

$$\mathcal{K}(r_0, r) = \sum_i d_i(r_0)K^i_{c_s^2,\rho}(r). \tag{1.20}$$

The determination of inversion coefficients and averaging kernels is influenced by the chosen inversion method and the potential parameters involved in the process. In fact, the inversion can be considered as a means to obtain coefficients and averaging kernels that yield the maximum amount of information. The averaging kernels serve as indicators of the resolution of the inversion. Ideally, it is desirable to achieve sharply peaked averaging kernels around a specific point $r = r_0$, while minimizing their amplitude far away from that point. Two commonly utilized inversion techniques are the Regularized Least Squares (RLS) method and the Optimally Localized Averages (OLA) method. The RLS method aims to determine the profiles of $\delta c_s^2/c_s^2$ and $\delta\rho/\rho$ that best fit the data by minimizing residuals and reducing uncertainties. On the other hand, the aim of the OLA method is not to fit the data, but rather to find linear combinations of frequency differences that result in a localized average of the unknown function through corresponding kernels, while also keeping the uncertainties small. More detailed information on the implementation of these techniques can be found in Basu (2016).
Once one has $\delta c_s^2/c_s^2 = (c^2_{s,\odot} - c^2_{s,\mathrm{model}})/c^2_{s,\odot}$ it is possible to invert the relation and find the values for $c^2_{s,\odot}$ since the model values are known. Basu et al. (2000) showed that the inferred values for the Sun depend very little on the reference model, and are thus considered a reliable description of the internal structure of the Sun.

1.4.2 Helioseismology results and the solar abundance problem

The early observation of high degree modes, which are trapped in the outer layer of the Sun, allowed to obtain information on the adiabatic structure of these layers, in particular on the depth of the convective envelope, which is estimated to be $R_{CZ} = (0.713 \pm 0.001)\,\mathrm{R}_\odot$ (Basu and Antia, 1997).
More recent observations of modes of all degrees, together with the inversion technique described in the previous section, allowed to obtain much more detailed information about the internal structure of the Sun. Figure 1.2 shows the profile of $\delta c_s/c_s$ obtained via helioseismic inversion in the solar interior for the chemical compositions presented in Table 1.1. For all the models the differences never exceed ~ 0.010, meaning data and model agree within 1%. The differences are however significant: all models share a peak just below the convective zone, and through the years the better determination of the chemical composition and the opacity profile of the solar interior only worsened the discrepancy, going from the excellent agreement of GS98 composition to the maximum difference of AGSS09. These inferences show that most recent models, including C11 and AAG21, are inadequate. MBS22 composition seems to restore the agreement with helioseismic data, obtaining results comparable to those of GS98. There are thus

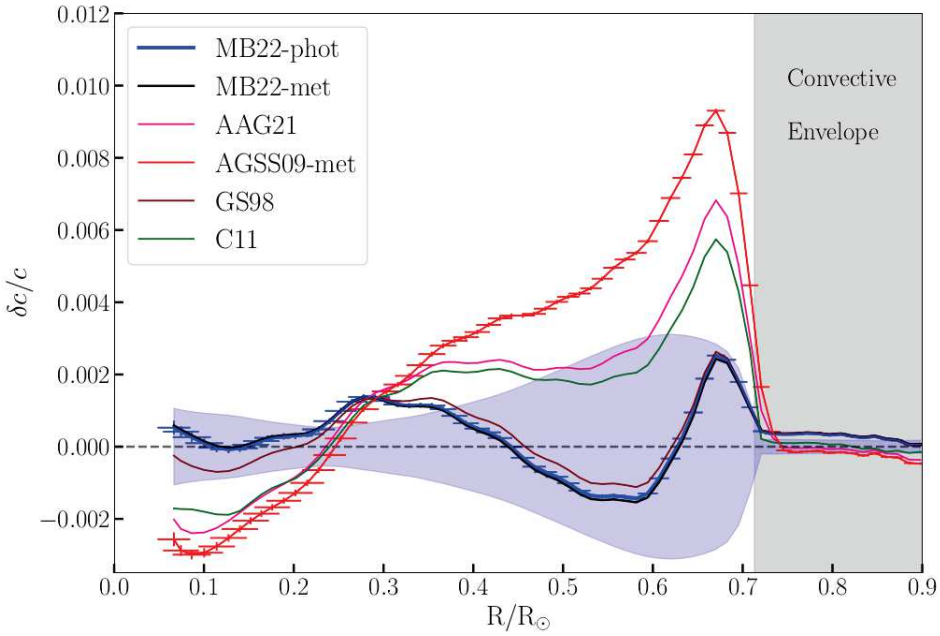

Figure 1.2. Differences of sound speed, in the sense (Sun) − (model), in the solar interior obtained via helioseismic inversion for the different chemical compositions presented in Table 1.1. The shaded blue area represents the MBS22 model uncertainties arising from the inputs to the model. Plot from Magg et al. (2022).

large differences between high-Z and low-Z models, with high-Z models giving better agreement with helioseismic data. These differences commonly go under the name of solar abundance problem.
Most seismic probes do not directly depend on the composition of the Sun, but rather on its opacity profile, which is a combined result of atomic calculations for the EoS and the chemical abundances. Christensen-Dalsgaard et al. (2009) computed a low-Z SSM with *ad hoc* adjustments so that the opacity profile mimics a high-Z models, while the chemical composition remains low-Z, obtaining results practically indistinguishable from those of a high-Z model. This means seismology cannot constrain opacity or compositions separately.

1.4.3 Possible solutions to the solar abundance problem

Since helioseismic results primarily depend on the opacity profile rather than on the chemical composition alone, there are a few possible ways out.
The first one is to question the determination of the low-Z abundances. 3D-RHD atmosphere models offer a good physical description of the solar photosphere, and different 3D-RHD models are in good agreement with each other. Thus it did not seem possible to restore a high-Z chemical composition, at least without a revision of the atomic physics involved in spectral lines formation, as was done for MBS22.
A possible alternative is that mixing processes in SSMs are not correct, and there are additional processes affecting the chemical composition such that it resembles a high-Z abundance in solar interior, while the surface composition remains low-Z. Examples of such processes are an increased element diffusion (Montalbán et al., 2004) and early ac-

cretion events in the solar system evolution (Guzik and Mussack, 2010; Serenelli et al., 2011). However, none of them offers a complete solution to the solar abundance problem.

The last possibility is to question the opacity determination. Villante (2010) showed that if the low-Z solar composition is adopted, adjustments of the order of $15 - 20\%$ in the radiative opacity are necessary to restore agreement between helioseismology and SSMs, while Villante et al. (2014) performed a global analysis including SSMs uncertainties, helioseismology and solar neutrinos, finding that there is no freedom in SSMs that can compensate the reduction of the metallicity other than the increase of the opacity. The experimental determination of opacities under solar conditions is particularly difficult due to the combination of high temperatures and densities. To accurately replicate the conditions present in the solar interior, experiments need to reach at least the less extreme conditions found at the base of the convective envelope, where the temperature is approximately $T \simeq 2.35 \times 10^6\,\mathrm{K}$ and the density is around $\rho \simeq 0.2\,\mathrm{g\,cm^{-3}}$, with an electron number density of $n_e \simeq 10^{23}\,\mathrm{cm^{-3}}$. Reaching these conditions experimentally remains a challenge, although recent results have approached them closely. This seems to indicate that an improvement in the opacity determination is indeed possible, and might be a way to solve the solar abundance problem.

Chapter 2

Changing Fe opacity in SSMs

Motivated by the fact that an increase in the radiative opacity could restore the agreement between SSMs and helioseismology, as showed by Villante (2010), and that there is room for an improvement in the opacities determination, I decided to investigate the effects of an increase of the radiative opacity on SSMs. In particular increased values for iron opacity are investigated. Iron plays a crucial role in solar opacities, contributing approximately 25% to the total opacity at the base of the convective envelope. Consequently, it significantly influences the seismic properties of SSMs (see Villante et al., 2014). This is due to iron being both abundant in the Sun and with a complex atomic structure. Recently at the Z-facility at Sandia labs (Bailey et al., 2015) an experiment showed that at conditions really close to those of the bottom of the convective envelope the Rosseland mean opacity for iron is on average 60% larger than the value predicted from atomic calculations. When experimental results are combined with atomic calculations the overall Rosseland mean is $\sim 7\%$ larger than the OP value used in SSMs. It is important to note that the conditions achieved at the Z-facility are not yet equivalent to those at the base of the convective zone, in particular the electron density is still approximately 2.5 times lower. However, there is clear evidence indicating that radiative opacities in atomic calculations could be underestimated by a significantly larger fraction than what differences between various theoretical calculations would suggest. In particular, the increase in Fe opacity alone found by Bailey et al. (2015) could be enough, if extrapolated to solar conditions, to restore the agreement between SSMs and helioseismology when C11 composition is used. This suggests that increasing the Fe opacity could improve the tension between SSMs and helioseismology.

2.1 Methods

In order to investigate the effect of an increase in opacity, several different SSMs realized with *ad hoc* opacity tables are calibrated. Opacity tables are obtained coupling the OPAL tables[1] or the TOPS tables[2] for the chosen chemical composition at high temperature $4.0 \leq \log(T/\mathrm{K}) \leq 8.7$ with the opacities calculated with the latest version of the ÆSOPUS code (Marigo and Aringer, 2009; Marigo et al., 2022) at low temperature $3.2 \leq \log(T/\mathrm{K}) \leq 4.0$. Apart from one model obtained using C11 abundances,

[1] `http://opalopacity.llnl.gov/`

[2] `https://aphysics2.lanl.gov/`

Table 2.1. Characteristics of the different models realized for this work. Last column represents the multiplicative factor for iron opacity.

Model	Chemical composition	Opacity	Fe multiplicative factor
C11	C11	OPAL	
MBS22	MBS22	OPAL	
FE1	MBS22	TOPS	1
FE2	MBS22	TOPS	2
FE3	MBS22	TOPS	3
FE4	MBS22	TOPS	4
FE5	MBS22	TOPS	5
FE7	MBS22	TOPS	7

the reference chemical composition is the new MBS22. Table 2.1 summarizes the main characteristics of the realized models, labeled as C11, MBS22 (as the used chemical composition) and FEn, as the Fe opacity multiplicative factor. The increase in iron opacity is achieved by multiplying the opacity value by a numeric multiplicative factor n, reported in the last column of the table. Figure 2.1 illustrates the logarithm of the ratio between the opacity of the different FEn models and OPAL opacities as a function of the temperature T and the variable $R = \rho T_6^{-3}$, with $T_6 = T/10^6\,\mathrm{K}$. In general TOPS opacities are lower than OPAL opacitites in the majority of the $R - T$ plane, and they become comparable when the multiplicative factor is between 4 and 7. At low temperature $3.2 \leq \log(T/\mathrm{K}) \leq 4.0$ all plots show a vertical white band, representing no difference in the chosen opacities, coming from the fact that in both cases in this temperature range the opacities are obtained with ÆSOPUS. Apparently, a good correspondence between the OPAL and TOPS opacities can be obtained when using a multiplicative factor around $3 - 4$.

2.1.1 SSMs with PARSEC

All the models used in this work are realized with PARSEC, PAdova and TRieste Stellar Evolution Code (Bressan et al., 2012). Given the initial composition Z_{ini} and Y_{ini} and the mixing length α, PARSEC solves the stellar evolution equations and computes an evolutionary track for the model from the Pre-Main Sequence (PMS) phase up to a given point. For solar models the computation was stopped at 5.5 Gyr. Convection is treated according to the MLT, while nuclear reaction rates are taken from the JINA REACLIB database. For the realized models the envelope overshooting parameter is set to zero.

2.1.2 Calibration technique

Each realized SSM needs to be calibrated, i.e. one has to find the appropriate values of Y_{ini}, Z_{ini} and α that reproduce the characteristics of the Sun at its present age $t_\odot$, as briefly described in Section 1.3. Table 2.2 summarizes the main characteristics of the Sun that can be compared with model predictions, together with the reference they are taken from. The surface abundances depend on the reference chemical composition for the model.

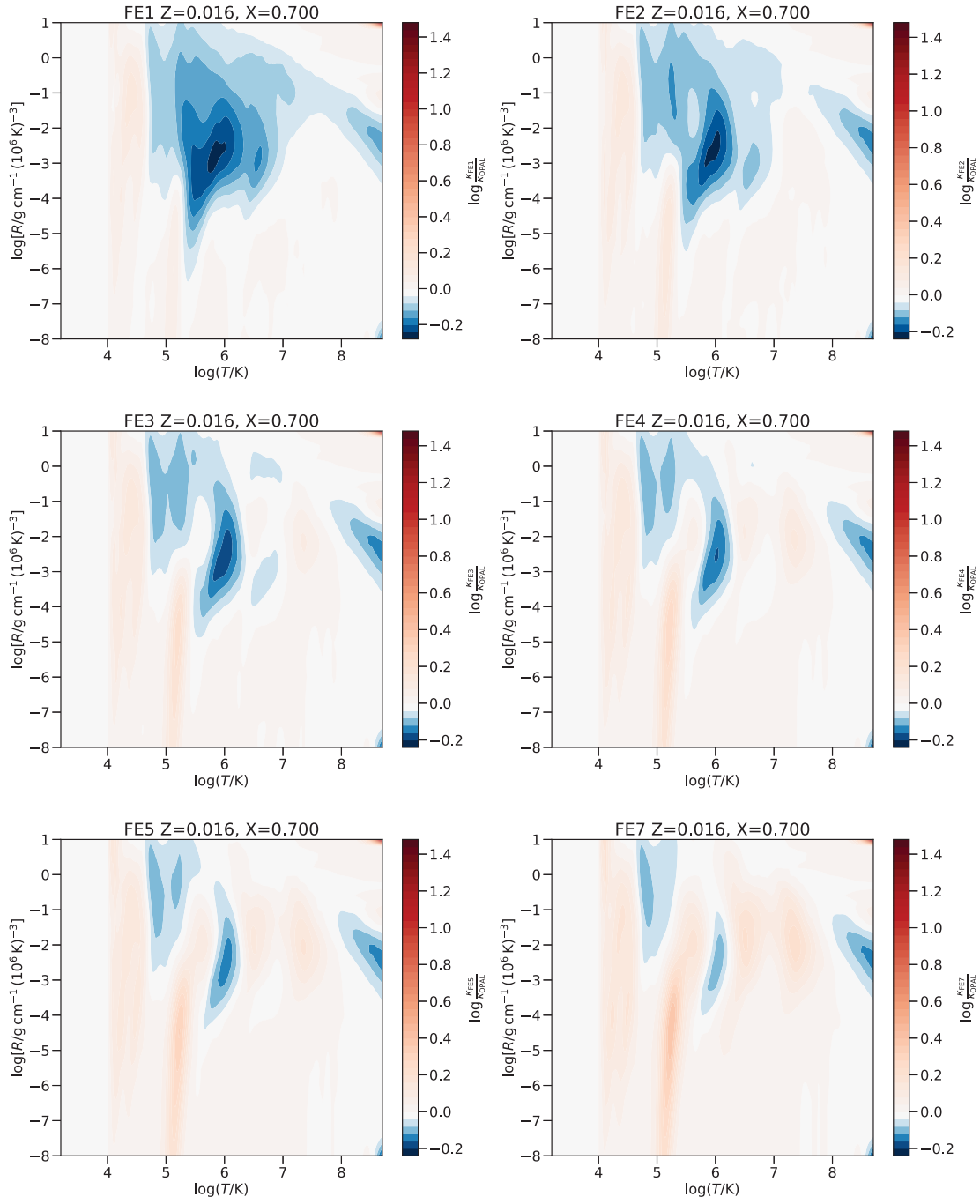

Figure 2.1. Differences in Rosseland mean opacities obtained form the OPAL and the TOPS project for the different models FE*n*.

Table 2.2. Observable quantities used for solar calibration. The surface abundances depend on the reference chemical composition. $R_{\rm ADI}$ is the radial coordinate at which there is the transition of ∇ from radiative to adiabatic, $\rho_{\rm ADI}$ is the density at $R_{\rm ADI}$ and $c_{s,\rm ADI}$ is the adiabatic sound speed at $R_{\rm ADI}$.

Solar data	Chemical composition C11	Chemical composition MBS22	Source
$M_\odot$ [10^{33} g]	1.989	1.989	From Kepler's third law
$t_\odot$ [Gyr]	4.566(5)	4.566(5)	Bahcall et al. (1995)
$L_\odot$ [erg s^{-1}]	3.846(5)	3.846(5)	Guenther et al. (1992)
$T_{\rm eff,\odot}$ [K]	5778(8)	5778(8)	From $L_\odot$ and $R_\odot$
$Y_\odot$	0.2485(35)	0.2485(35)	Basu and Antia (2004)
$Z_\odot$	0.0152(15)	0.0165(14)	Caffau et al. (2011) - Magg et al. (2022)
$(Z/X)_\odot$	0.0207(15)	0.0225(14)	Caffau et al. (2011) - Magg et al. (2022)
$R_\odot$ [10^{10} cm]	6.960(1)	6.960(1)	Guenther et al. (1992)
$R_{\rm ADI}/R_\odot$	0.713(1)	0.713(1)	Basu and Antia (1997)
$\rho_{\rm ADI}$ [g cm^{-3}]	0.192(7)	0.192(7)	Basu et al. (2009)
$c_{s,\rm ADI}$ [10^7 cm s^{-1}]	2.23(2)	2.23(2)	Basu et al. (2009)

The adopted calibration procedure is a bit different from usual, in the sense that it has four free parameters: the usual initial chemical composition $Y_{\rm ini}$ and $Z_{\rm ini}$ and mixing length α and then the age of the model, which is left as a free parameter. Calibrating the model thus means also finding the best value for the age of the model at which the model observables match the observed solar quantities. I will call the observables of the model the physical quantities $(L, T_{\rm eff}, Y_{\rm surf}, Z_{\rm surf}, (Z/X)_{\rm surf}, R, R_{\rm ADI}, \rho_{\rm ADI}, c_{s,\rm ADI})$, which are to be compared to those reported in Table 2.2. $Z_{\rm surf}$, $Y_{\rm surf}$ and $(Z/X)_{\rm surf}$ represent surface abundances. The table also reports the solar mass, which is a fixed parameter for the models, and the estimated solar age.
The best values for the four parameters $\theta = (\text{age}, Z_{\rm ini}, Y_{\rm ini}, \alpha)$ are found using a Markov-Chain Monte Carlo (MCMC) algorithm. MCMC methods are a class of algorithms for sampling from a probability distribution, that can also be used in inference for finding the model that best fits a given set of data. They are particularly useful in determining robust uncertainties on the parameters of the model and in exploring the correlation between these parameters. The distribution to be sampled is the posterior distribution $p(\theta|x)$ of a certain parameter θ given the data x, which is obtained from Bayes theorem

$$p(\theta|x) = \frac{p(\theta)p(x|\theta)}{p(x)}, \tag{2.1}$$

with $p(\theta)$ the prior distribution of the parameter, $p(x|\theta)$ the likelihood of the model and $p(x)$ the evidence, representing just a normalization factor.
A prerequisite of these algorithms is the ability to predict the model observables for any given combination of the parameters in the parameter space, which is needed to evaluate the likelihood. Calculating an evolutionary track for each step of the MCMC algorithm would be too computationally expensive, so this problem was solved as follows. For each model many evolutionary tracks with different combinations of $Z_{\rm ini}$, $Y_{\rm ini}$ and α are realized. In particular $Z_{\rm ini}$ is chosen between 0.012 and 0.020 in steps of 0.001,

$Y_{\rm ini}$ is chosen between 0.25 and 0.31 in steps of 0.01 and α is chosen between 1.5 and 2.2 in steps of 0.175. So a total number of $9 \times 7 \times 5 = 315$ tracks are calculated for each model. These boundaries are chosen to give acceptable values of the solar observables: models with an age lower than 4 Gyr or higher than 5 Gyr are not acceptable, while the initial helium and metal abundances must certainly be higher than the present solar value, since both surface helium and metal abundances decrease during the evolution because of gravitational settling. This sets a robust lower bound for $Y_{\rm ini}$, while because of the uncertainties on the solar chemical composition I decided to explore a larger region of the initial metallicity parameter space, setting the lower bound to 0.012.
For each track the values of the observables at given values of the age of the model are collected in a table, the age chosen between 4.0 Gyr and 5.2 Gyr in steps of 0.02 Gyr. This table is used to construct an interpolator, that can predict the values of the model observables at any point in the parameter space linearly interpolating between all the calculated tracks.
Once the problem of calculating the model at any given point of the parameter space is solved, the MCMC analysis is carried out as follows. At the beginning an initial set of L walkers $\boldsymbol{\theta}(t) = \{\theta_1(t), \ldots, \theta_L(t)\}$ is defined, where each walker represents a random point $(\text{age}, Z_{\rm ini}, Y_{\rm ini}, \alpha)$ in the parameter space. The walkers begin exploring the parameter space taking a given number of steps N. At each step a proposal for a move $\theta_k(t) \to \theta_k(t+1)$ for each walker in another point of the parameter space is done. The new position can be accepted with a certain acceptance probability that depends on how well the model in this new point describes the data. The likeliness of the model at a given point of the parameter space is numerically accounted for by the likelihood distribution, which is related to the model χ^2 as

$$\ln \mathcal{L}(\theta) = -\frac{\chi^2}{2} = -\frac{1}{2}\sum_i \left(\frac{\text{model}_i(\theta) - \text{data}_i}{\sigma_i}\right)^2, \tag{2.2}$$

the sum running over all the observables of the model. σ_i is the uncertainty of the i-th observable, reported in Table 2.2. The uncertainties for L and $T_{\rm eff}$ are different from those of the table, and are fixed to 0.01%. In this way, the luminosity and effective temperature have a higher weight with respect to the other observables, and the algorithm is forced to reproduce them with high precision.
The MCMC checks the ratio of the likelihood $\ln \mathcal{L}(\theta_k(t+1)) / \ln \mathcal{L}(\theta_k(t))$. If the new location produces a better match to the data, the walker moves there and repeats the process. If the new location is worse, it retreats to its previous position and tries a new direction. Sometimes even when a new position is good the walker stays put, or if the new position is bad, the walker goes, depending on the acceptance probability. This makes sure that walkers do not get trapped on individual peaks of high probability. As many steps are done the walkers explore the parameter space, and eventually they begin climbing towards the maximum of the probability distribution. Once all the steps are performed the first 20% of the walkers' positions are discarded. This is done because the first part of the chain is an adjustment part, where the walkers almost freely explore the space in search of the maximum posterior position. This means the first terms are not necessarily representative of the posterior distribution, so a common practice is to discard them. Figure 2.2 shows the behavior of the walkers in the MCMC calibration of my MBS22 model. The first steps of the walkers randomly explore the parameter space, and only after a few iterations the walkers start to move towards the region of highest

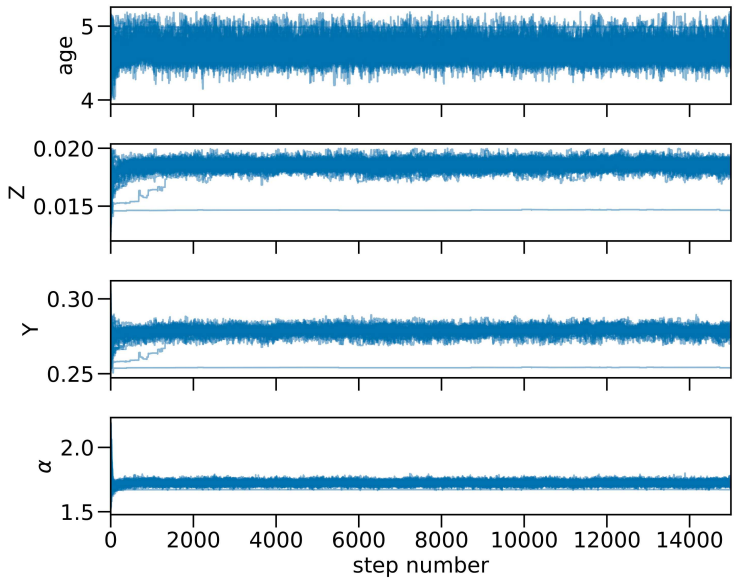

Figure 2.2. Positions of the walkers during the calibration of model MBS22. Z and Y refer to the initial values.

probability, stopping the exploration of the regions of low probability. There is also one walker who got stuck, rejecting all move proposals and never moving until the end of the simulation.
At the end of the process one has the posterior distributions for all the parameters of the model. The median of the posterior distribution represents the value of the parameter that gives a model best describing the data, while the uncertainties are given by the 16 and 84 percentiles. The posterior distributions can also be used to calculate joint distributions and analyze the correlation between the parameters.
The MCMC analysis is carried out with python `emcee` package (Foreman-Mackey et al., 2013), which makes use of the Metropolis-Hastings algorithm and proposes moves for the walkers with the "stretch move" method by Goodman and Weare (2010), moving $L = 50$ walkers randomly initialized in the parameter space by $N = 15\,000$ steps. The prior distributions for the four parameters are assumed to be uniform over the parameter space.
The whole calibration procedure can be repeated adding new evolutionary tracks for points in the parameter space closer to the maximum of the posterior distribution, in order to improve the performance of the interpolator and refine the results of the calibration.

2.1.3 Internal structure

Once each model was calibrated, I computed an evolutionary track for the model using the best fit values of the parameters obtained from the calibration. This allows to have more accurate values for the model observables rather than relying on the approximate values given by the interpolator. Furthermore, for each model it is possible to calculate the internal structure and plot the profiles of $\delta c_s^2/c_s^2$ and $\delta\rho/\rho$ using as reference values the helioseismic ones, in order to see if the model has improved the agreement with

helioseismology. The variations are calculated in the sense (Sun − model), and the reference values for the solar quantities are those presented by Basu et al. (2009) from the Birmingham Solar Oscillation Network (BiSON) experiment.

2.2 Results

2.2.1 OPAL opacities: C11 and MBS22 models

Both MBS22 and C11 models are particularly interesting, the former because it is obtained with MBS22 chemical composition, which was only recently published, and the latter because an analogous calibration was performed by Bressan et al. (2012) with PARSEC using the same observational data. Differences between that calibrated model and my C11 model are thus due to the different version of PARSEC used, since the code has undergone some improvement during the last decade.
Figures 2.3 and 2.4 show the posterior distributions resulting from the MCMC for C11

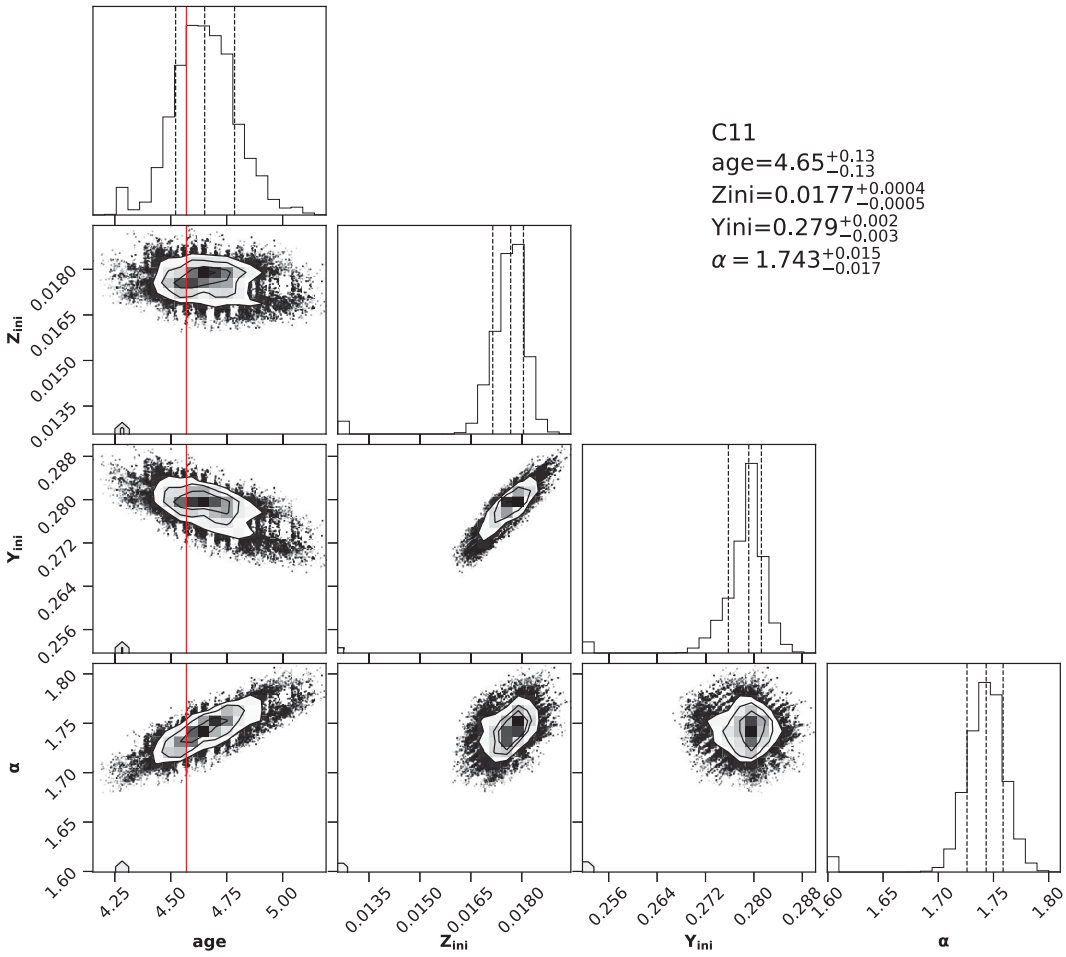

Figure 2.3. Posterior distributions for the four parameters (age, $Z_{\rm ini}$, $Y_{\rm ini}$, α) with their best estimates for model C11. The red line represents the reference value for the age of the Sun $t_\odot$.

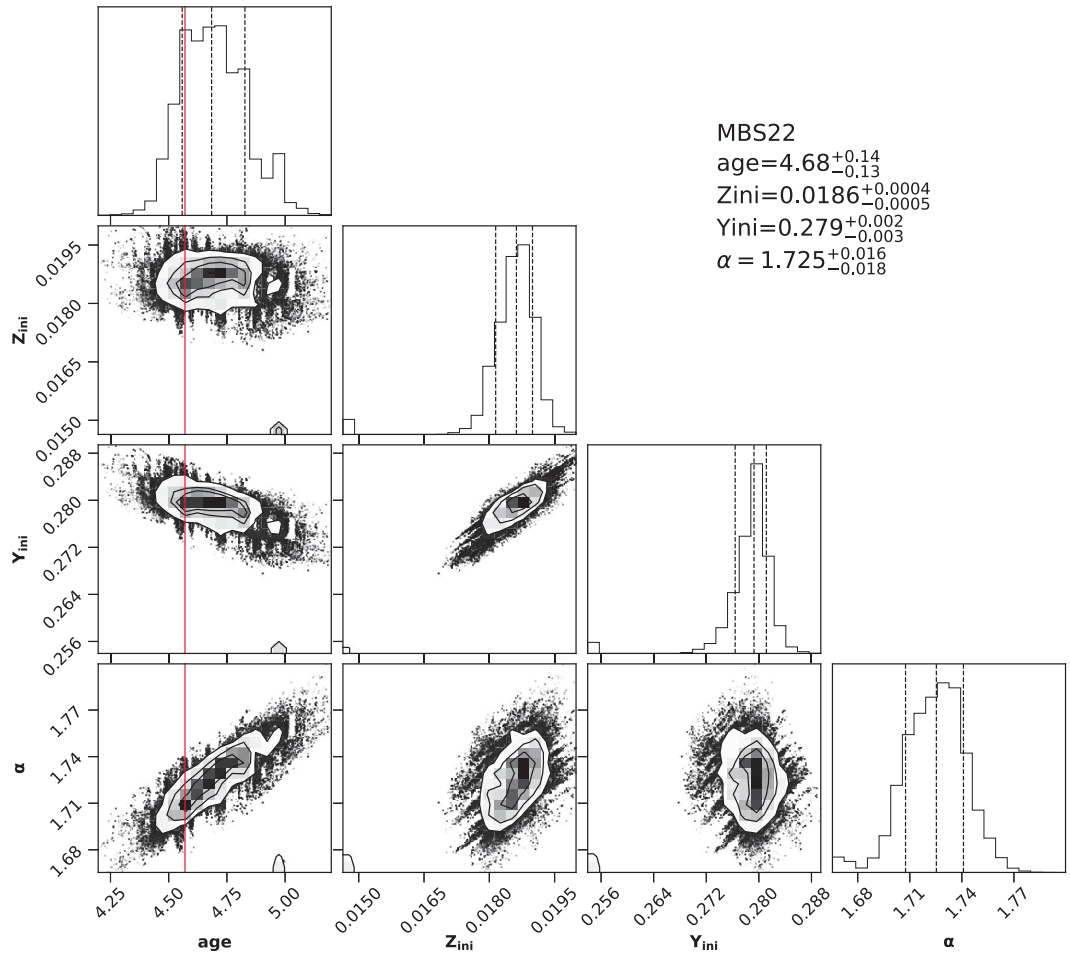

Figure 2.4. Posterior distributions for the four parameters $(\text{age}, Z_{\text{ini}}, Y_{\text{ini}}, \alpha)$ with their best estimates for model MBS22. The red line represents the reference value for the age of the Sun $t_\odot$.

and MBS22 models. In all C11 contour plots there are some values on the lower left corner, probably given by a walker that got stuck in that point of the parameter space. A similar situation happens in MBS22 contour plots, with a walker stuck on the boundary of the parameter space. Both figures show direct correlation between Z_{ini} and Y_{ini}, consistently with the fact that increasing Y_{ini} leads to a more luminous star, and to balance the increasing luminosity Z_{ini} needs to increase as well. Similarly, the inverse correlation between Y_{ini} and the age of the model shown in the figure can be explained by the fact that increasing the luminosity, related to Y_{ini}, the model arrives at the solar value sooner during its evolution, so the age of the model decreases. Finally, the plots show direct correlation between the mixing length α and the age of the model.
Table 2.3 summarizes the main characteristics of my models and of Bressan et al. (2012) model. All the quantities of C11 model are consistent with those found by Bressan et al. (2012). The last row of the table reports the reduced χ^2 of the models, which indicate good agreement between both models and the available data. The age of both the models is consistent with the measured one of $t_\odot = (4.566 \pm 0.005) \times 10^9$ yr, at a level of

Table 2.3. Main characteristics of Bressan et al. (2012) model and C11 and MBS22 models. MCMC parameters are listed with their uncertainties. The last row is the reduced χ^2 of my models.

Observable	Bressan et al. (2012)	C11	MBS22
age [Gyr]	4.593	4.65 ± 0.13	$4.68^{+0.14}_{-0.13}$
$Z_{\rm ini}$	0.01774	$0.0177^{+0.0004}_{-0.0005}$	$0.0186^{+0.0004}_{-0.0005}$
$Y_{\rm ini}$	0.28	$0.279^{+0.002}_{-0.003}$	$0.279^{+0.002}_{-0.003}$
α	1.74	$1.743^{+0.015}_{-0.017}$	$1.725^{+0.016}_{-0.018}$
L [erg s^{-1}]	3.848	3.844	3.845
$T_{\rm eff}$ [K]	5779	5777	5778
$Y_{\rm surf}$	0.24787	0.24813	0.24824
$Z_{\rm surf}$	0.01597	0.01600	0.01681
$(Z/X)_{\rm surf}$	0.02169	0.02174	0.02287
R [10^{10} cm]	6.9584	6.9589	6.9576
$R_{\rm ADI}/R$	0.7125	0.7139	0.7139
$\rho_{\rm ADI}$ [g cm^{-3}]	0.1887	0.1893	0.1920
$c_{s,\rm ADI}$ [10^7 cm s^{-1}]	2.2359	2.2336	2.2336
$\chi^2_{\rm red}$		0.38	1.04

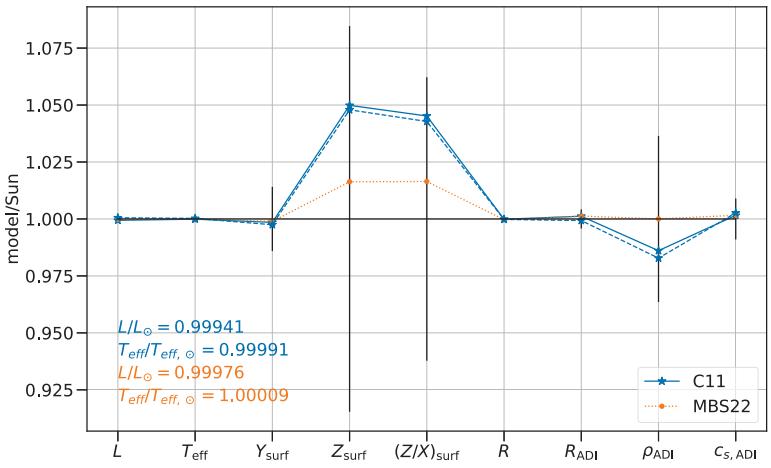

Figure 2.5. Ratio between the model characteristics and the corresponding solar value. Symbols are as follows. Blue stars and solid line: C11 model; blue stars and dashed line: Bressan et al. (2012) model; yellow dots and dotted line: my MBS22 model. The black line represents the solar values of Table 2.2 with their uncertainties. The first two blue values of the ratios $L/L_\odot$ and $T_{\rm eff}/T_{\rm eff,\odot}$ are for my C11 model, the second two in yellow are for my MBS22 model.

0.7σ (C11 model) and 1σ (MBS22 model). Figure 2.5 shows the values of the different observables for the three models compared to the solar quantities. The reported values of $L/L_\odot$ and $T_{\rm eff}/T_{\rm eff,\odot}$ indicate that both models reproduce the observed luminosity and effective temperature with a precision of a few 10^{-4}. All the observables are at $< 1\sigma$ from the solar data, apart from the radius of MBS22 model, which is at $\sim 3\sigma$ from the measured value. The metallicity of C11 and MBS22 models is a bit higher than the

solar value, while the density at the bottom of the convective envelope is a bit lower for C11 model. Both features are shared between C11 model and Bressan et al. (2012) model. Overall there is no significant discrepancy between these two models. Both my models have an optimum agreement with the observable data and can be accepted as good models for the Sun.

The left-hand panel of Figure 2.6 shows the relative adiabatic sound speed variation $\delta c_s^2/c_s^2$ in the sense (Sun−model) as a function of the radial coordinate inside the Sun for my models C11 (blue solid line) and MBS22 (yellow dotted line). The solar values are obtained from BiSON data (Basu et al., 2009). In the same figure there are Bressan et al. (2012) model (blue dashed line), Basu et al. (2009) model differences with respect to Michelson Doppler Imager (MDI) data using GS98 abundances (green dashed line) and Serenelli et al. (2009) profiles using GS98 abundances (red dash-dotted line) and AGSS09 abundances (purple solid line) for comparison. The right-hand panel shows the relative density variation $\delta\rho/\rho$ profile for my C11 and MBS22 models, and for Bressan et al. (2012) and Basu et al. (2009) models. Apart from the innermost and outermost regions, my C11 model performs quite well regarding the sound speed profile, at a comparable level with Basu et al. (2009) and Serenelli et al. (2009) models with GS98 abundances. Also MBS22 model is quite accurate, even though the sound speed in the middle region is a bit more overestimated than C11 model, while it has a less pronounced decrease close to the bottom of the convective envelope. The comparison between my C11 model and Bressan et al. (2012) model regarding the sound speed profile shows small variations, with my new model performing a little worse in the innermost region and a little better close to the convective envelope. The density profile instead has a worse behavior, with both my models underestimating the density in the inner-

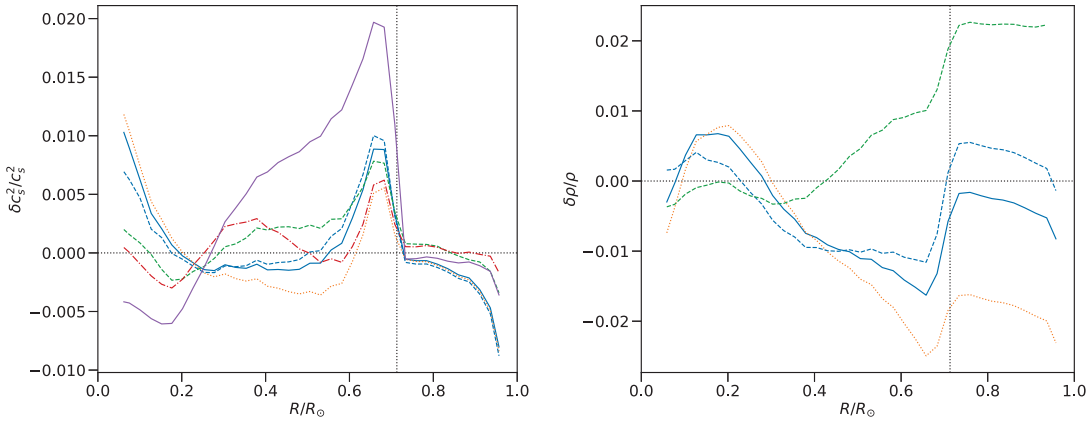

Figure 2.6. Left-hand panel: interior relative differences (in the sense Sun minus model) in the squared sound speed $\delta c_s^2/c_s^2$. Solar values are obtained from BiSON data (Basu et al., 2009). Symbols are as follows. Blue solid line: my C11 model; blue dashed line: Bressan et al. (2012) model; yellow dotted line: my MBS22 model; green dashed line: Basu et al. (2009) model using GS98 solar abundances; red dash-dotted line: Serenelli et al. (2009) model using GS98 solar abundances; purple solid line: Serenelli et al. (2009) model using AGSS09 solar abundances. Right-hand panel: interior relative differences for the density profile $\delta\rho/\rho$. In this case only Basu et al. (2009) model is shown for comparison. In both panels the dotted black vertical line represents the radial coordinate of the bottom of the convective envelope.

most regions and overestimating it elsewhere. In this case my C11 model and Bressan et al. (2012) model behave a bit differently, in particular in the convective region, where they exhibit an opposite behavior.

2.2.2 TOPS opacities: FEn models

Figures A.1 to A.6 in Appendix A show the results of the MCMC algorithm for the various FEn models. The two cases FE1 and FE2 both exhibit the same behavior, with walkers getting stuck on the boundary of the parameter space. Figures 2.7 and 2.8 show the behavior of the walkers in MCMC calibration of these two models as a function of the number of iterations. Both figures show how the walkers looked for regions of higher metallicity in the parameter space, getting stuck in the upper boundary trying to reach even higher values. Such a high $Z_{\rm ini}$ would result in a too high $Z_{\rm surf}$ at the present day age of the Sun, meaning these two models produce no acceptable solution. This is probably due to TOPS FE1 and FE2 opacities being too low, and since the opacity is low the model tries to go to higher metallicity to compensate for the missing opacity contribution. This would suggest that these two cases have too low opacity to explain the observed characteristics of the Sun. Figure 2.7 also shows how $Y_{\rm ini}$ got stuck on the lower boundary of the parameter space, and the fact that the helium abundance could not decrease anymore is related to the age not increasing above a certain value, generating a boundary effect even if the age walker is located in the middle of the parameter space. This is consistent with the inverse correlation between $Y_{\rm ini}$ and the age of the model.
Moving to models FE3 to FE7, all of them give acceptable solutions in the parameter space. All the plots show the same behavior as C11 and MBS22 models, with direct correlation between $Z_{\rm ini}$ and $Y_{\rm ini}$ and between the age and α, and inverse correlation

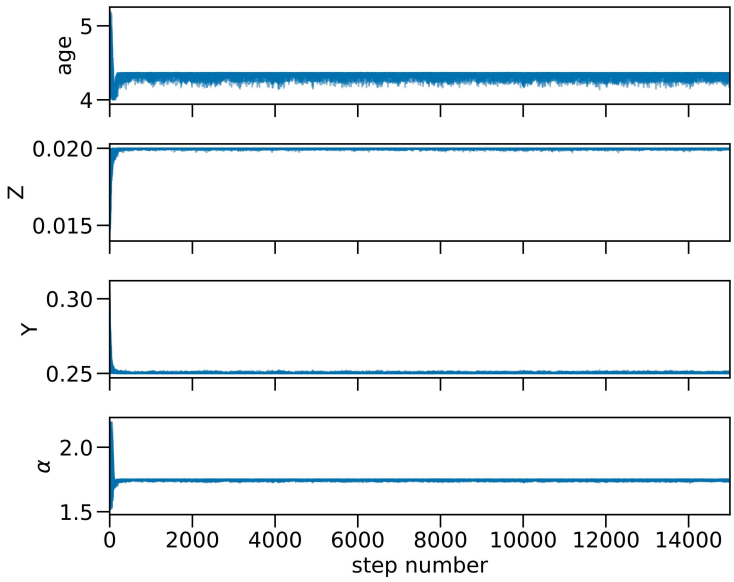

Figure 2.7. Positions of the walkers during the calibration of model FE1. Z and Y refer to the initial values.

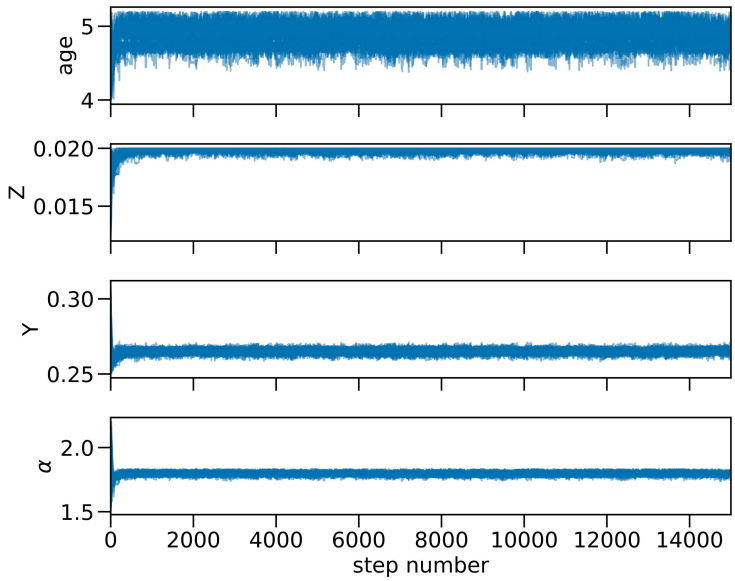

Figure 2.8. Positions of the walkers during the calibration of model FE2. Z and Y refer to the initial values.

between $Y_{\rm ini}$ and the age of the model.
Table 2.4 reports the values of the observables of FEn models, while Figure 2.9 shows the ratio between these observables and the reference solar value. In both cases there is no FE1 or FE2 model, because no acceptable solution was found in the parameter space. The values of $L/L_\odot$ and $T_{\rm eff}/T_{\rm eff,\odot}$ suggest that all the models are quite descriptive of these two fundamental solar quantities, with differences from few 0.01% to few 0.1%. As already noted, the initial metallicity $Z_{\rm ini}$ of the models decreases with increasing opacity, in order to compensate for the missing contribution. Moreover during hydrogen burning the surface metallicity decreases, mainly because of gravitational settling, so lowering the initial metallicity results in a lower surface value at the best age of the model. On the contrary the initial helium abundance $Y_{\rm ini}$ increases with increasing opacity and decreasing $Z_{\rm ini}$, as if trying to keep constant the initial hydrogen abundance $X_{\rm ini}$. This might be related to the fact that the value $X_{\rm ini}$ determines how much fuel is available for hydrogen burning, which is directly linked to the age of the model. Since all models need to arrive at roughly half the main sequence to be representative of the Sun, the age (and so $X_{\rm ini}$ is somehow fixed). Increasing $Y_{\rm ini}$ then results in an increased surface helium $Y_{\rm surf}$ at the best age of the model. This suggests that there is no way for models FE5 and FE7 to match the observed surface abundances: at their best age they both have a surface helium higher than the solar value and a surface metallicity lower than the solar value. Adjusting the metallicity would require increasing $Z_{\rm surf}$ and thus $Z_{\rm ini}$, but since $Z_{\rm ini}$ and $Y_{\rm ini}$ are directly proportional this would mean increasing also $Y_{\rm ini}$, so $Y_{\rm surf}$ would increase as well, worsening the agreement with the reference value. The same reasoning applies when trying to decrease $Y_{\rm surf}$.
Models FE3 and FE4 on the other hand give both good agreement with the reference solar values. The high $\chi^2_{\rm red}$ of FE3 model is mainly due to the radius value, which is at roughly 3σ from the reference value. Nevertheless, all the other parameters of the

model have optimal agreement with the reference value, suggesting that this model could be accepted.
Finally, the age of all the models is $\sim 2\sigma$ higher than the reference solar value, and it increases with the opacity, even though the initial helium abundance increases and the age and $Y_{\rm ini}$ are inversely correlated, so these models are hardly acceptable as a good description of the Sun. Models with higher multiplicative factors for the opacity, like FE5 and FE7, overestimate the solar age too much and surely cannot be accepted. Nevertheless, the fact that all models overestimate the solar age, even if within the 3σ

Table 2.4. Main characteristics of FEn models. MCMC parameters are listed with their uncertainties. The last row is the reduced χ^2 of the models.

Observable	FE3	FE4	FE5	FE7
age [Gyr]	$4.78^{+0.11}_{-0.12}$	$4.79^{+0.10}_{-0.12}$	4.85 ± 0.13	$4.92^{+0.12}_{-0.10}$
$Z_{\rm ini}$	0.0187 ± 0.0004	0.0167 ± 0.0004	0.0148 ± 0.0004	$0.0125^{+0.0003}_{-0.0002}$
$Y_{\rm ini}$	$0.278^{+0.003}_{-0.002}$	0.283 ± 0.003	0.284 ± 0.003	0.289 ± 0.002
α	1.747 ± 0.013	$1.696^{+0.011}_{-0.012}$	$1.651^{+0.014}_{-0.011}$	$1.589^{+0.010}_{-0.011}$
L [erg s^{-1}]	3.844	3.845	3.849	3.833
$T_{\rm eff}$ [K]	5775	5778	5779	5777
$Y_{\rm surf}$	0.24726	0.25116	0.25286	0.25750
$Z_{\rm surf}$	0.01689	0.01501	0.01338	0.01131
$(Z/X)_{\rm surf}$	0.02296	0.02046	0.01824	0.01546
R [10^{10} cm]	6.9636	6.9581	6.9602	6.9508
$R_{\rm ADI}/R$	0.7152	0.7143	0.7146	0.7123
$\rho_{\rm ADI}$ [g cm^{-3}]	0.1944	0.1973	0.1971	0.2056
$c_{s,\rm ADI}$ [10^7 cm s^{-1}]	2.2254	2.2309	2.2291	2.2436
$\chi^2_{\rm red}$	3.21	1.43	3.47	27.5

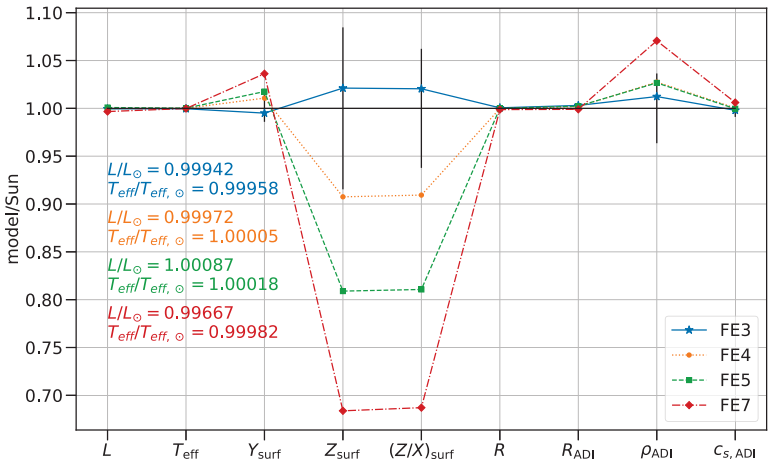

Figure 2.9. Ratio between the model characteristics and the corresponding solar value. Symbols are as follows. Blue stars and solid line: FE3 model; yellow dots and dotted line: FE4 model; green squares and dashed line: FE5 model; red diamonds and dash-dotted line: FE7 model. The black line represents the solar values of Table 2.2 with their uncertainties. The values of the ratios $L/L_\odot$ and $T_{\rm eff}/T_{\rm eff,\odot}$ are associated to the model described by the same color.

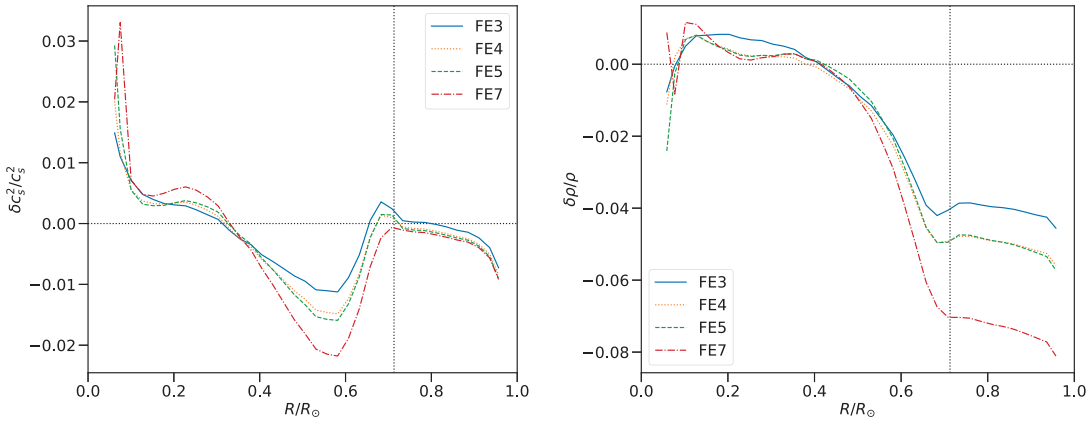

Figure 2.10. Left-hand panel: interior relative differences (in the sense Sun minus model) in the squared sound speed $\delta c_s^2/c_s^2$. Right-hand panel: interior relative differences for the density profile $\delta\rho/\rho$. Solar values are obtained from BiSON data (Basu et al., 2009). Symbols are as follows. Blue Solid line: FE3 model; yellow dotted line: FE4 model; green dashed line: FE5 model; red dash-dotted line: FE7 model. In both panels the dotted black vertical line represents the radial coordinate of the bottom of the convective envelope.

boundary, suggests that there might be something missing in the treatment of the models.

Figure 2.10 shows the internal profiles of the relative variation of the adiabatic sound speed $\delta c_s^2/c_s^2$ and of the density $\delta\rho/\rho$ as a function of the radial coordinate for FE3 to FE7 models. The left-hand panel shows how the discrepancy with the reference profile gets worse with increasing opacity, with FE3 being the model that best agrees with the helioseismic constraints. For all the models the peak just below the bottom of the convective envelope has disappeared, while there is a broad region in which the sound speed is largely above the reference helioseismic value. This is the opposite of what was found for models MBS22 and C11, where between $0.35\,R_\odot$ and $0.7\,R_\odot$ the sound speed was close to the solar value, and presented a peak just below the convective zone. In the innermost region of the Sun instead models with higher opacity give an underestimated sound speed, with a discrepancy of $2-3\%$. Model FE3 is also the one with the best density profile above the FEn models, as shown in the right-hand panel. All models are close to the helioseismic reference in the region between $0.1\,R_\odot$ and $0.35\,R_\odot$, while from that point on the density of the models increases and the discrepancy with the helioseismic value gets worse, resulting in a $4-8\%$ difference in the convective envelope.

Overall, models FE3 and FE4 are the ones best describing the Sun, but the overestimated age and the discrepancy in sound speed and density profiles suggests that there is still room for improving the model. Moreover, when also C11 and MBS22 models are taken into account, it seems that the OPAL opacities still offer a better physical description, without the need for an increase in the iron contribution.

2.2.3 Envelope overshooting

SSMs have been able to describe the proprieties of the Sun without the need of envelope overshooting (Basu et al., 1994; Christensen-Dalsgaard et al., 1995). However, the

recent results of Christensen-Dalsgaard et al. (2011) suggest that it might be possible to include envelope overshooting in the description of the Sun. Motivated by this, I decided to realize some solar models including the envelope overshooting parameter Λ_e as a free parameter of the MCMC simulations, to be determined together with the age, the initial composition and the mixing length. In this case the age parameter space was chosen between 3.8 Gyr and 5.0 Gyr in steps of 0.1 Gyr. The larger step in the age parameter space is necessary because of computational reasons, since including a new parameter in the MCMC algorithm increases exponentially the computational time. Λ_e was chosen between zero and 0.4 in steps of 0.1. The models taken into consideration are MBS22, FE2, FE3, FE4 and FE5. All these models show an overestimation of the solar age. Moreover FE*n* models exhibit a sound speed profile with opposite behavior with respect to what was found for my OPAL MBS22 and C11 models and for Bressan et al. (2012) model, suggesting that these models may require some improvement.
Figures B.1 to B.5 in Appendix B show the results of the MCMC algorithm for these overshooting models. FE2 model in this case presents a solution in the parameter space, unlike in the previous case without overshooting, with $\Lambda_e \sim 0.28$, although the posterior for this parameter is not sharply peaked. The age of the model is 2.5σ below the measured age $t_\odot$, making the model hardly acceptable for a suitable description of the Sun. FE3 and MBS22 models have a solution within 1σ form the correct age and can be accepted. Their prediction for the overshooting parameter is $\Lambda_e = 0.093$ and $\Lambda_e = 0.062$ respectively. In both cases the posterior for Λ_e is peaked slightly above zero, suggesting that a moderate amount of overshooting might improve the model. Models FE4 and FE5 also predict a solar age within 1σ from the measured value, making these models acceptable in principle, but they both show a posterior distribution for Λ_e peaked to-

Table 2.5. Main characteristics of the models realized calibrating the overshooting parameter Λ_e. MCMC parameters are listed with their uncertainties. The last row is the reduced χ^2 of the models.

Observable	MBS22	FE2	FE3	FE4
age [Gyr]	$4.47^{+0.19}_{-0.20}$	$3.97^{+0.27}_{-0.22}$	$4.47^{+0.21}_{-0.30}$	$4.65^{+0.19}_{-0.21}$
$Z_{\rm ini}$	$0.0181^{+0.0006}_{-0.0007}$	0.0189 ± 0.0006	$0.0180^{+0.0006}_{-0.0009}$	$0.0161^{+0.0005}_{-0.0004}$
$Y_{\rm ini}$	$0.279^{+0.002}_{-0.003}$	0.270 ± 0.002	$0.279^{+0.002}_{-0.004}$	$0.281^{+0.004}_{-0.002}$
α	$1.692^{+0.027}_{-0.045}$	$1.674^{+0.076}_{-0.083}$	$1.703^{+0.029}_{-0.049}$	$1.672^{+0.024}_{-0.029}$
Λ_e	$0.062^{+0.075}_{-0.042}$	$0.280^{+0.076}_{-0.083}$	$0.093^{+0.098}_{-0.057}$	$0.051^{+0.063}_{-0.037}$
L [erg s^{-1}]	3.847	3.830	3.849	3.852
$T_{\rm eff}$ [K]	5779	5775	5782	5780
$Y_{\rm surf}$	0.24935	0.24511	0.25016	0.25078
$Z_{\rm surf}$	0.01643	0.01744	0.01639	0.01459
$(Z/X)_{\rm surf}$	0.02238	0.02365	0.02234	0.01986
R [10^{10} cm]	6.9570	6.9508	6.9509	6.9592
$R_{\rm ADI}/R$	0.7123	0.7102	0.7154	0.7149
$\rho_{\rm ADI}$ [g cm^{-3}]	0.1893	0.1841	0.1879	0.1920
$c_{s,\rm ADI}$ [10^7 cm s^{-1}]	2.2415	2.2417	2.2256	2.2277
$\chi^2_{\rm red}$	2.25	23.5	20.2	1.94

wards zero, indicating a preference for no overshooting. Model FE5 in particular shows an initial chemical composition which is the same as the case with no overshooting. For this reason I decided to discard this model for the following analyses, while I still kept track of model FE4.

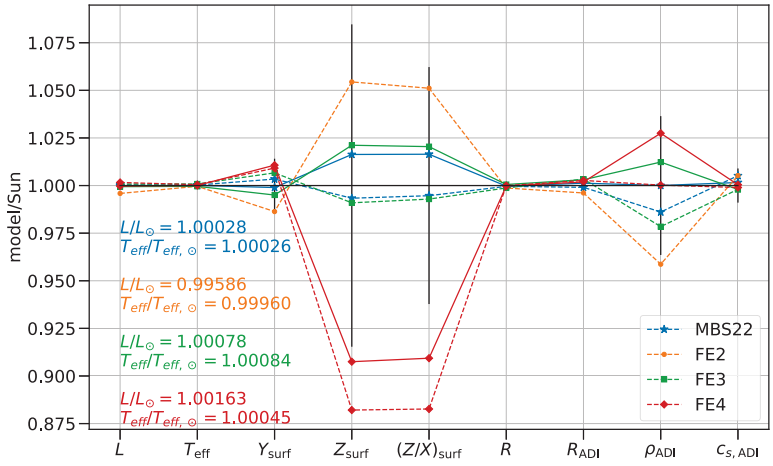

Figure 2.11. Ratio between the model characteristics and the corresponding solar value. In all cases the dashed line indicates the model with overshooting, while the solid line represents the model without overshooting (i.e. with $\Lambda_e = 0$) discussed in the previous section (when available). Symbols are as follows. Blue stars: MBS22 model; yellow dots: FE2 model; green squares: FE3 model; red diamonds: FE4 model. The black line represents the solar values of Table 2.2 with their uncertainties. The values of the ratios $L/L_\odot$ and $T_{\rm eff}/T_{\rm eff,\odot}$ are associated to the model with overshooting described by the same color.

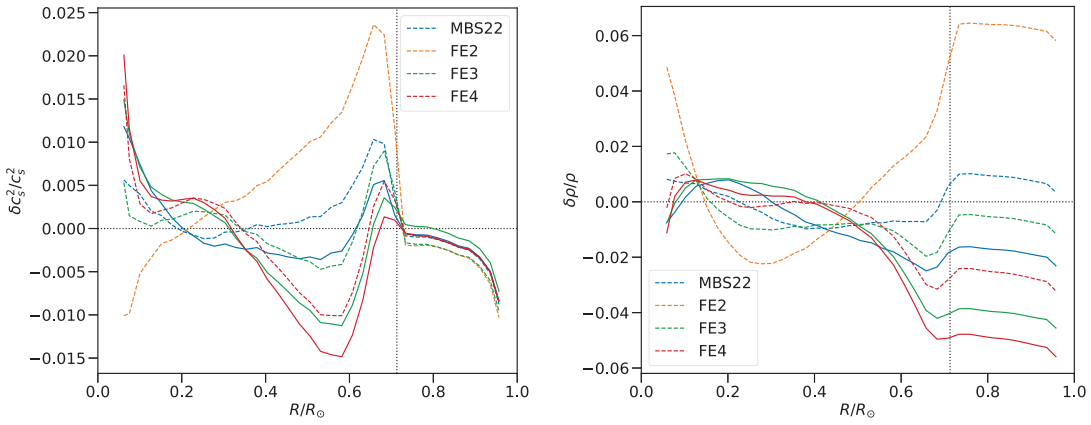

Figure 2.12. Left-hand panel: interior relative differences (in the sense Sun minus model) in the squared sound speed $\delta c_s^2/c_s^2$. Right-hand panel: interior relative differences for the density profile $\delta\rho/\rho$. Solar values are obtained from BiSON data (Basu et al., 2009). Symbols are as follows. Blue line: MBS22 model; yellow line: FE2 model; green line: FE33 model; red line: FE4 model. Dashed lines represent models with overshooting, while solid lines of the same color are the models with the same opacity but without overshooting discussed in the previous section (when available). In both panels the dotted black vertical line represents the radial coordinate of the bottom of the convective envelope.

Table 2.5 reports the values of the observables of these overshooting models, while Figure 2.11 shows the ratio between the observables and the reference solar value. Dashed lines represent models with overshooting, while solid lines of the same color are the models with the same opacity but without overshooting, discussed in the previous section (when available). Model FE2 is not able to describe the solar luminosity, which is well measured and together with the effective temperature is a fundamental parameter in calibrating solar models. MBS22, FE3 and FE4 models instead both reproduce $L_\odot$ and $T_{\mathrm{eff},\odot}$ within few $\sim 0.1\%$ accuracy, whit MBS22 touching $\sim 0.03\%$ accuracy.
The most notable effects of envelope overshooting are a reduction of Z_{surf}, $(Z/X)_{\mathrm{surf}}$ and ρ_{ADI} with respect to models without overshooting. In the case of FE4 model, this results in a surface metallicity that seems too low to be able to well describe a model with the high-Z MBS22 chemical composition, despite the reduced χ^2 of the model being the smallest of the four. Model FE3 instead has a high χ^2 because of the radius prediction, which is $\sim 9\sigma$ below the measured value. Apart from the radius however model FE3 describes solar luminosity, effective temperature and chemical composition quite well, at a comparable level with MBS22 model, which seems the best model of the four.
Figure 2.12 shows the internal profiles of the relative variation of the adiabatic sound speed $\delta c_s^2/c_s^2$ and of the density $\delta\rho/\rho$ as a function of the radial coordinate for the four overshooting models. Both panels show how model FE2 cannot reproduce the solar profile. For models MBS22, FE3 and FE4 the introduction of overshooting has improved both the density and the sound speed profiles. The peak in the sound speed profile below the convective zone appears again, with an amplitude of $\sim 0.1\%$ comparable to that of many other models in literature. In all the other regions the sound speed profile difference for MBS22 and FE3 models is below 0.5%. The same applies to the density profile, with MBS22 and FE3 models giving the best result, even better than my MBS22 model with no overshooting, with differences with respect to solar values lying below 1% almost everywhere. Model FE4 has undergone some improvement as well thanks to the introduction of overshooting, describing the density profile almost perfectly in the region $0.2 \leq R/R_\odot \leq 0.5$, but failing in representing the solar behavior in the convective region.
From this analysis it seems that introducing some envelope overshooting in the models can indeed lead to better results, with MBS22 and FE3 models being the ones showing the best description of the Sun.

Chapter 3

Solar neutrinos

The Sun is powered by a chain of nuclear reactions, with the net result of hydrogen being burnt into helium. Some of these reactions produce neutrinos, which do not interact with matter and can escape freely from the Sun, traveling to the Earth, where their flux can be measured. Each reaction provides a characteristic neutrino spectrum, so measuring the different fluxes can help in understanding which are the dominant reactions ongoing in the Sun and what is their contribution to the total solar energy. Moreover, the comparison between the measured flux and the predictions given by SSMs can offer a valuable test of our understanding of the Sun.

3.1 Main sources of solar neutrinos

I will give a brief description of the main reactions that produce neutrinos in the Sun following Bahcall (1989). There are eight nuclear reactions responsible for the production of solar neutrinos, five in the pp-chain and three in the CNO-cycle. Equations (3.1) and (3.2) show the different reactions of these two hydrogen burning mechanisms, highlighting the reactions which produce neutrinos. The most abundant neutrinos

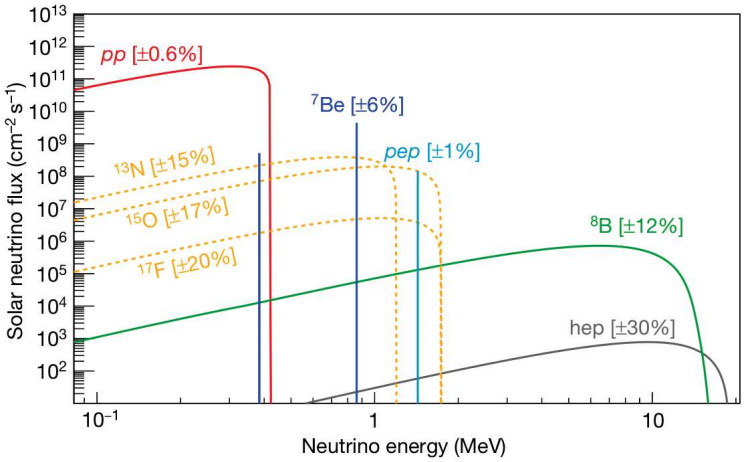

Figure 3.1. Solar neutrino energy spectrum taken from Borexino Collaboration et al. (2018). The flux is given in units of $\mathrm{cm}^{-2}\,\mathrm{s}^{-1}\,\mathrm{MeV}^{-1}$ for continuum sources and in $\mathrm{cm}^{-2}\,\mathrm{s}^{-1}$ for monoenergetic sources. Numbers in square brackets are 1σ uncertainties.

come from the pp reaction, but they have low energy ($q \leq 0.420\,\text{MeV}$, with q being the neutrino energy). Figure 3.1 shows the solar neutrino energy spectrum predicted from SSMs obtained by the Borexino Collaboration et al. (2018). The pp neutrino spectrum increases slowly up to a maximum at $\sim 0.31\,\text{MeV}$ and then cuts off quickly. ^{8}B and hep spectra are more symmetric and more energetic, with peaks at $\sim 6.4\,\text{MeV}$ and $\sim 9.6\,\text{MeV}$ and extended tails. pep and ^{7}Be neutrinos produce monoenergetic spectra, with $q = 1.442\,\text{MeV}$ for the pep neutrino and $q = 0.862\,\text{MeV}$ (89.7%) or $q = 0.384\,\text{MeV}$ (10.3%) for the ^{7}Be neutrino.

pp-chain

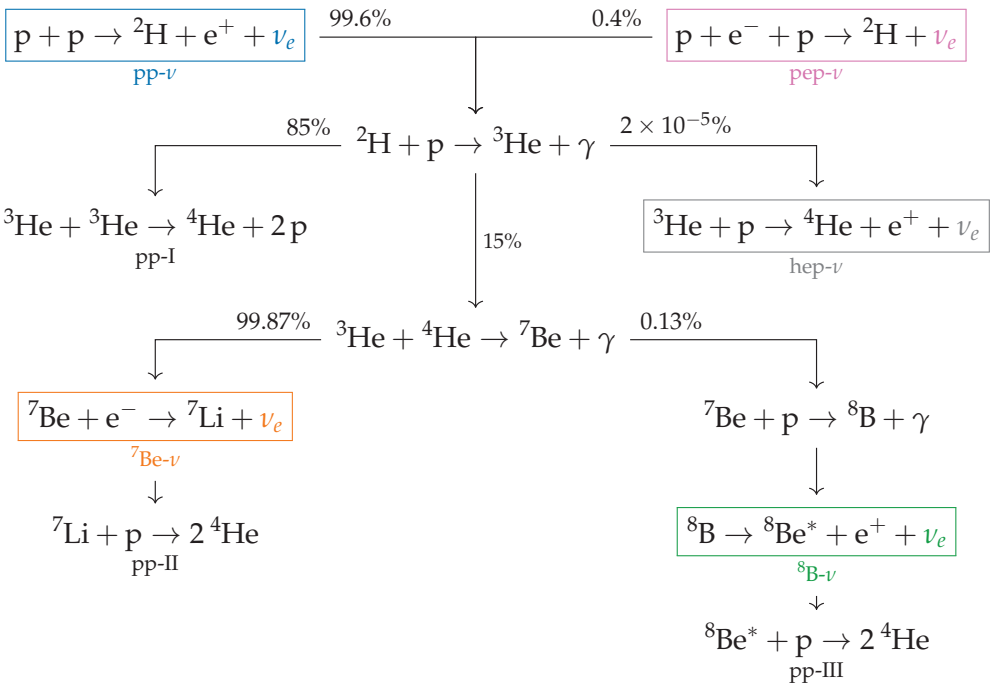

(3.1)

CNO-cycle

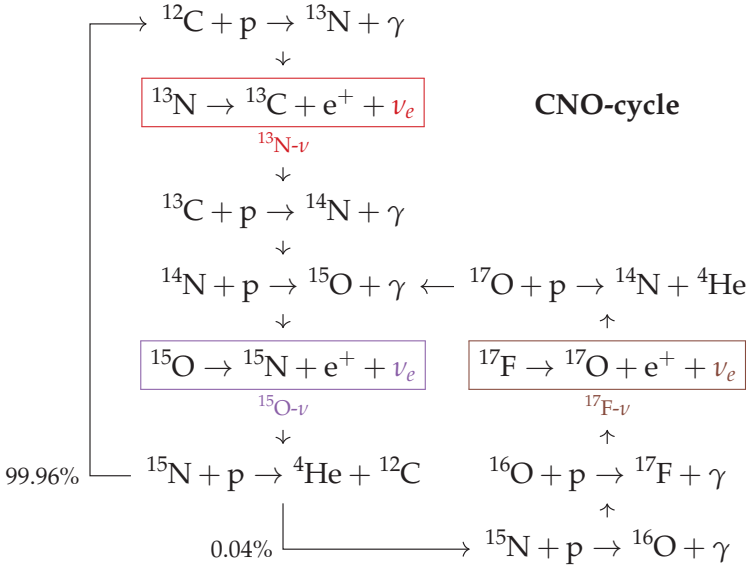

(3.2)

CNO energy spectra have the same shape as the pp neutrino spectrum, but they are more difficult to measure since only few CNO reactions are ongoing in the Sun. ^{8}B and hep neutrinos, although being only a tiny fraction of the total neutrinos emitted by the Sun, are the most energetic ones, which in principle makes them easier to detect on Earth. Most of the experiments are primarily sensitive to ^{8}B neutrinos. CNO neutrinos have low energy and are too scarce to be detected consistently, making their flux difficult to evaluate.

3.2 Solar neutrino fluxes

During the last years many efforts were done to improve the determination of the flux of solar neutrinos. Bergström et al. (2016) collected and analyzed data from many neutrino experiments, giving some predictions for the flux for the different solar neutrinos of the pp-chain and giving upper bounds for the flux of CNO neutrinos. Some improvement from those data has been done recently by the Borexino collaboration, with new up-to-date flux measurements for the pp, pep, ^{7}Be and ^{8}B neutrinos (Borexino Collaboration et al., 2018) and a first measurement of the total CNO neutrino flux (Appel et al., 2022). However Bergström et al. (2016) values for the fluxes are widely used in literature, so I will take them as the reference solar value for a comparison with my results.
I calculated the pp, ^{7}Be, ^{8}B and the three CNO neutrino fluxes, while I do not provide an estimate for the pep and hep neutrinos, because PARSEC does not include these two reactions in its nuclear network.

3.2.1 My models' predictions

I calculated the predicted neutrino luminosity integrating the local production rate r_i for each neutrino over the mass of the Sun as

$$L_{\nu_i} = \int_0^M r_i(m, T, \rho, \dots)\, \mathrm{d}m. \tag{3.3}$$

The flux at the Earth is then obtained by dividing the previous value by $4\pi d^2$ with $d = 1$ AU. The first part of Table 3.1 shows the values for the different neutrino fluxes for my C11, MBS22 and FEn models, including overshooting models. They are all realized using JINA REACLIB reaction rates. Almost all the models reproduce closely the pp neutrino flux (within $\sim 1\sigma$) and meet the conditions for CNO neutrinos. Exceptions are FE5 and FE7 models, which perform poorly in reproducing all neutrino fluxes. These models were not successful in reproducing the solar observables and the sound speed and density profiles either, confirming they are not suitable for a good description of the Sun. Regarding ^{7}Be and ^{8}B neutrinos, all the models give predictions that are greater than the solar value, with differences between $7 - 30\%$ for ^{7}Be and $8 - 80\%$ for ^{8}B. The more the opacity increases, the farther the model predictions are from solar values. Overshooting models seem to perform a little better than models without overshooting. The fact that ^{7}Be and ^{8}B fluxes are systematically overestimated suggests that there might be something missing in the treatment of the models, and that there is room for some improvement.

Table 3.1. Neutrino fluxes at 1 AU of the different realized models. -ovr models are the models with non-zero overshooting discussed in Section 2.2.3. Solar values are taken from Bergström et al. (2016). V17 values are from Vinyoles et al. (2017) taking as reference a high-Z (HZ) or low-Z (LZ) chemical composition. Units are 10^{10} (pp), 10^{9} (^{7}Be), 10^{8} (^{13}N, ^{15}O) and 10^{6} (^{8}B, ^{17}F) cm^{-2} s^{-1}. The first half of the table refers to models using JINA reaclib rates for ^{7}Be electron capture, while the second half refers to models using Vescovi et al. (2019) rate for ^{7}Be electron capture.

Flux	Φ(pp)	$\Phi(^{7}\mathrm{Be})$	$\Phi(^{8}\mathrm{B})$	$\Phi(^{13}\mathrm{N})$	$\Phi(^{15}\mathrm{O})$	$\Phi(^{17}\mathrm{F})$
Solar	$5.971^{+0.037}_{-0.033}$	$4.80^{+0.24}_{-0.22}$	$5.16^{+0.13}_{-0.09}$	≤ 13.7	≤ 2.8	≤ 85
V17 (HZ)	$5.98(1 \pm 0.006)$	$4.93(1 \pm 0.06)$	$5.46(1 \pm 0.12)$	$2.78(1 \pm 0.15)$	$2.05(1 \pm 0.17)$	$5.29(1 \pm 0.20)$
V17 (LZ)	$6.03(1 \pm 0.005)$	$4.50(1 \pm 0.06)$	$4.50(1 \pm 0.12)$	$2.04(1 \pm 0.14)$	$1.44(1 \pm 0.16)$	$3.26(1 \pm 0.28)$
			JINA rates			
C11	5.94	5.38	6.18	3.26	2.54	5.02
MBS22	5.93	5.40	6.15	3.69	2.89	4.96
MBS22-ovr	5.97	5.15	5.62	3.39	2.58	4.40
FE3	5.89	5.77	7.61	4.26	3.47	6.08
FE3-ovr	5.96	5.33	6.55	3.69	2.89	5.00
FE4	5.87	5.93	8.30	3.98	3.27	5.79
FE4-ovr	5.92	5.72	7.72	3.66	2.96	5.20
FE5	5.86	6.12	8.82	3.71	3.11	5.55
FE7	5.78	6.25	9.14	3.28	2.82	5.10
			Vescovi et al. (2019) rates			
C11	5.94	4.97	8.97	3.26	2.54	5.02
MBS22	5.93	4.99	9.02	3.69	2.89	4.96
MBS22-ovr	5.97	4.77	8.17	3.39	2.58	4.40
FE3	5.89	5.36	11.12	4.26	3.47	6.08
FE3-ovr	5.96	5.12	9.98	3.69	2.89	5.00
FE4	5.87	5.75	12.61	3.98	3.27	5.79
FE4-ovr	5.92	5.49	11.29	3.66	2.96	5.20
FE5	5.86	5.90	12.96	3.71	3.11	5.55
FE7	5.78	6.07	13.28	3.28	2.82	5.10

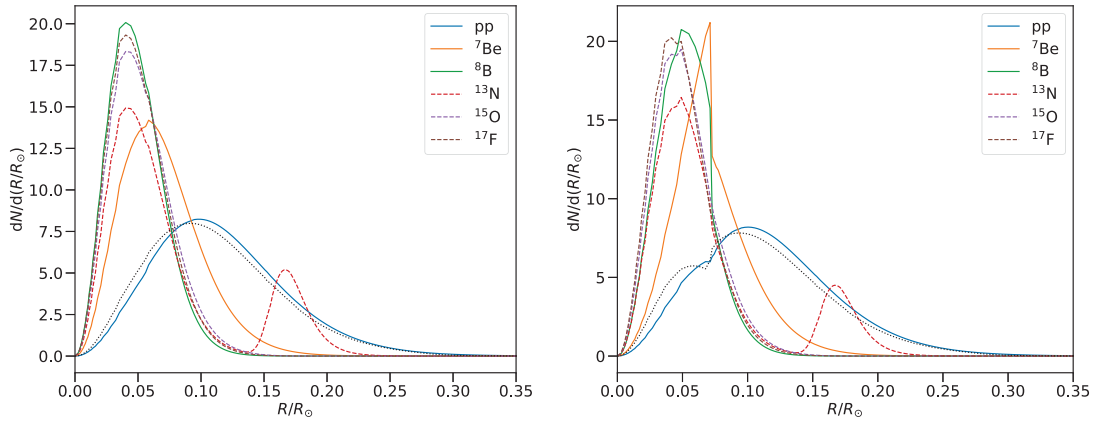

Figure 3.2. Differential neutrino generation rate in neutrinos per second for the different reactions for models FE3 (left-hand panel) and FE7 (right-hand panel), both without envelope overshooting. Solid lines are neutrinos from the pp-chain, while dashed lines represent neutrinos from the CNO-cycle. The black dotted line represents the differential luminosity $\mathrm{d}L/\mathrm{d}(R/R_\odot)$ produced at that radial coordinate. In both panels this luminosity follows closely the pp reaction rate.

Overall the best-performing models are MBS22, MBS22-ovr and FE3-ovr, which are the same models that best describe the solar observables and the sound speed and density profiles as well.
Figure 3.2 shows the local neutrino generation rate $\mathrm{d}N/\mathrm{d}(R/R_\odot)$, i.e. the number of neutrinos generated per each reaction per second at each radial coordinate as a function of the radial coordinate itself, for models FE3 (left-hand panel) and FE7 (right-hand panel). Similar plots for all the models can be found in Appendix C. The values for each reaction are normalized to the integrated total generation rate for that reaction. Most of the neutrinos are produced in the innermost region of the core for $R \lesssim 0.1\,\mathrm{R}_\odot$ because of their strong temperature dependence. Exceptions are represented by pp neutrinos, with a weaker temperature dependence than the other reactions, produced mostly between $0.05\,\mathrm{R}_\odot$ and $0.2\,\mathrm{R}_\odot$, with a peak at $\sim 0.1\,\mathrm{R}_\odot$, and by ^{13}N neutrinos, which have two separate peaks roughly at $0.05\,\mathrm{R}_\odot$ and $0.17\,\mathrm{R}_\odot$, the second peak being less important than the first one. The black dotted line represents the local luminosity $\mathrm{d}L/\mathrm{d}(R/R_\odot)$, which follows almost perfectly in both cases the pp production rate, confirming that this reaction is the main responsible for the emitted solar luminosity. The increase of iron opacity modifies the shape and the position of the peaks of ^{7}Be and ^{8}B rates. This effect might be related to a variation of the temperature, which is closely linked to the opacity.

3.2.2 Revised ^{7}Be electron capture rate

The prediction of neutrino fluxes in standard solar models is highly dependent on the reaction rates adopted. The inner regions of stars exhibit elevated temperatures and densities, meaning the atoms are almost completely ionized. Consequently, describing the matter within the stellar core requires the application of plasma physics. The decay of a specific isotope is significantly influenced by the plasma's density ρ and temperature T under such conditions. To calculate decay rates within stellar contexts it is essen-

tial to use precise plasma models. Recently Vescovi et al. (2019) presented a revised rate for the ^{7}Be electron capture which takes into consideration the screening effect of the surrounding plasma. This rate was calculated modeling the electron capture as a two body scattering problem, whose rate is proportional to the electron density ρ_e, which is screened and modified by the surrounding particles in the plasma. The expression of the modified rate is

$$\lambda\left(\frac{\rho}{\mu_e}, T_6\right) = \frac{\rho}{\mu_e}\frac{\kappa}{\sqrt{T_6}}\left[1 + \alpha(T_6 - 16) + \beta\frac{\rho}{\mu_e}(1 + \gamma(T_6 - 16))\right], \tag{3.4}$$

where ρ is the density in g cm^{-2}, T_6 is the temperature in units of 10^6 K, μ_e is the electron mean molecular weight and κ, α, β and γ are some constants (see Vescovi et al., 2019,

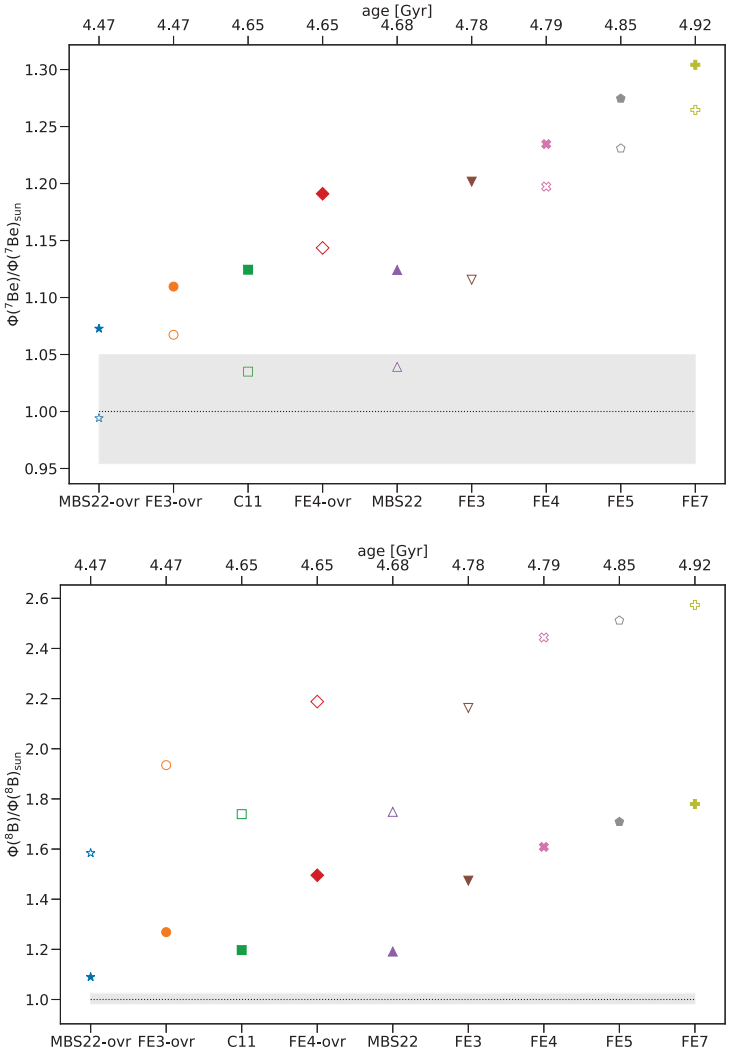

Figure 3.3. Ratio between the neutrino flux predicted from each model and the solar reference value for ^{7}Be-ν (upper panel) and ^{8}B-ν (lower panel). Filled markers represent models using JINA rate for ^{7}Be electron capture, while empty markers are models using Vescovi et al. (2019) revised rate. The gray band is the 1σ interval around the reference solar value. In both panels the models are ordered by growing age.

Table 2). The rate is related to the electron number density as $n_e = \rho/\mu_e m_p$, m_p being the mass of the proton.
The introduction of screening effects makes the electron capture on ^{7}Be less efficient, resulting in a lower reaction rate and a lower neutrino flux. This could have some beneficial effects on my models, all of which overestimate the ^{7}Be neutrino flux. The results from the computation of my models with this revised rate for this reaction are reported in the second half of Table 3.1. ^{7}Be neutrino fluxes with this revised rate are $3-8\%$ lower than the fluxes obtained using JINA rates and are closer to the solar value. In particular MBS22-ovr model reproduces almost perfectly the ^{7}Be flux, while C11, MBS22 and FE3-ovr models predictions are roughly at 1σ from the solar value. Conversely, the ^{8}B neutrino flux obtained with this revised rate for ^{7}Be electron capture has increased by $40-50\%$ with respect to models using JINA rates, going even farther from the solar value. This was expected, since the two main reactions ^{7}Be can undergo are proton capture $^7\mathrm{Be}(\mathrm{p},\gamma)^8\mathrm{B}$ (leading to a ^{8}B neutrino) and electron capture $^7\mathrm{Be}(\mathrm{e}^-,\nu_e)^7\mathrm{Li}$ (producing a ^{7}Be neutrino). Reducing the electron capture rate means more ^{7}Be nuclei are available for the other reaction, thus increasing the number of ^{8}B neutrinos. This behavior of the ^{7}Be and ^{8}B neutrino fluxes is shown in Figure 3.3. The upper panel shows the ratio between the ^{7}Be neutrino flux and the corresponding solar value for all my models, while the lower panel does the same for the ^{8}B flux. In both panels filled markers represent models with JINA rate, and empty markers represent models with the revised rate of Vescovi et al. (2019). Models are ordered by growing age. Both panels show the progressive worsening of the models as the opacity increases, confirming how models with high opacity are unable to describe the Sun. The upper panel shows that models that lie close to the solar value are models C11, MBS22, MBS22-ovr and FE3-ovr, with the revised rate performing better than JINA rate. The lower panel on the contrary shows that almost all models give values too far from the solar one. The closest model is MBS22-ovr, whose ^{8}B flux prediction is at 3.5σ for the solar value, being $\sim 9\%$ higher. In this case the revised rate performs definitely worse, and its predictions are incompatible with the measured flux.
The overall best-performing model is MBS22-ovr, followed by MBS22 and FE3-ovr. These models all give predictions at $\lesssim 2\sigma$ from the measured flux for ^{7}Be with JINA rates. Using Vescovi et al. (2019) revised rate gives better predictions for the ^{7}Be flux, but makes the ^{8}B flux totally incompatible with the measured one. This suggests that overall JINA REACLIB reaction rates perform better than Vescovi et al. (2019) revised rate.

3.3 About the age of the models

Even if it is not strictly related to solar neutrinos, the age of the models is a key parameter in the description of SSMs. Figure 3.3 shows the models ordered by their age, reported on the upper horizontal axis of each panel. The reference solar value for the age of the Sun is (4.556 ± 0.005) Gyr (Bahcall et al., 1995), which is a revision of the previously adopted (4.49 ± 0.04) Gyr (Guenther, 1989). Considering only the predicted values of the age and not their uncertainties (which are usually quite big for SSMs), only MBS22-ovr and FE3-ovr agree with the old measure of the age by Guenther (1989), while no model is in agreement with Bahcall et al. (1995) measure.
Increasing Fe opacity has the effect of increasing the age of the model, going farther and

farther from the reference value. However, the introduction of envelope overshooting has a significant effect: the age of the model decreases by $\Delta t \sim 0.30\,\mathrm{Gyr}$ ($\sim 7\%$) for FE3 model and by $\Delta t \sim 0.15\,\mathrm{Gyr}$ ($\sim 3\%$) for FE4 model. The overshooting parameter Λ_e for the two overshooting models is 0.093 and 0.051 respectively. Despite being small, it has a significant impact on the age of the models. This probably happens because of a balance between convective mixing and gravitational settling, which requires adjusting the age of the model to recover the correct values for the surface helium and metallicity. The new FE3-ovr and FE4-ovr models now have an age difference of $\sim 0.18\,\mathrm{Gyr}$ and bracket the solar reference value by Bahcall et al. (1995). This bracketing suggests that there might be a new model in between with an intermediate value for the Fe opacity whose age matches the reference solar value.

Chapter 4

Conclusions

Advancements in determining the solar chemical composition during the last years have had an adverse impact on the alignment between SSMs and helioseismology, with SSMs no longer aligning with helioseismic constraints. The restoration of the agreement would require either increasing the atomic opacity or returning to the previous higher metal abundances. The new high-Z chemical composition by Magg et al. (2022) alleviates the tension between SSMs and helioseismology, but the opacity still plays a key role: using either the OPAL or TOPS opacity tables has a drastic impact on SSMs realized adopted MBS22 chemical composition.

My model MBS22-ovr realized with OPAL opacities performs well in reproducing both the present-day solar observables (luminosity, effective temperature, surface composition) and the internal sound speed and density profiles. The best model among my models realized using TOPS opacities is model FE3-ovr, which performs at a comparable level to my MBS22-ovr model. Both these models have a small amount of envelope overshooting, $\Lambda_e = 0.062$ for MBS22-ovr and $\Lambda_e = 0.093$ for FE3-ovr. Models with the same opacity but with no envelope overshooting perform slightly worse in reproducing the sound speed and density profiles, in particular in the convective zone. When considering higher multiplicative values for Fe opacity, like 5 or 7, the models are unable to reproduce the present-day surface chemical composition of the Sun and the sound speed and density profiles, which worsen as the opacity increases, and even considering non-vanishing envelope overshooting does not fix these models.

Regarding solar neutrinos, MBS22-ovr and FE3-ovr models predict fluxes that are close to the measured ones, while models with different opacity multiplicative factors give inaccurate predictions. The pp neutrino flux prediction is close to the measured value, while the ^{7}Be and ^{8}B values are larger than the measured ones for both models. Considering the revised rate by Vescovi et al. (2019) for ^{7}Be electron capture improves the predictions of ^{7}Be neutrinos, but almost doubles the discrepancy between ^{8}B neutrino predictions and observations. This suggests that the adopted JINA REACLIB reaction rates still perform better. Still, there is room for the improvement of the models.

In conclusion, models with OPAL opacities are able to well reproduce what is known about the Sun, while models with TOPS opacities give an acceptable description with an increase of Fe opacity by a factor 3, and in both cases a small amount of envelope overshooting helps in improving the model. Such a multiplicative factor for TOPS opacities gives the closest values to the OPAL ones among the considered multiplicative factors, and this is probably the reason why FE3-ovr model resembles quite closely

MBS22-ovr model. This underlines the need for more accurate and reliable opacity determinations, in particular at the solar interior conditions.

Bibliography

M. Alongi, G. Bertelli, A. Bressan, and C. Chiosi. Effects of envelope overshoot on stellar models. *Astron. Astrophys.*, 244:95, Apr. 1991.

S. Appel, Z. Bagdasarian, D. Basilico, G. Bellini, J. Benziger, R. Biondi, B. Caccianiga, F. Calaprice, A. Caminata, P. Cavalcante, A. Chepurnov, D. D'Angelo, A. Derbin, A. Di Giacinto, V. Di Marcello, X. F. Ding, A. Di Ludovico, L. Di Noto, I. Drachnev, D. Franco, C. Galbiati, C. Ghiano, M. Giammarchi, A. Goretti, A. S. Göttel, M. Gromov, D. Guffanti, A. Ianni, A. Ianni, A. Jany, V. Kobychev, G. Korga, S. Kumaran, M. Laubenstein, E. Litvinovich, P. Lombardi, I. Lomskaya, L. Ludhova, G. Lukyanchenko, I. Machulin, J. Martyn, E. Meroni, L. Miramonti, M. Misiaszek, V. Muratova, R. Nugmanov, L. Oberauer, V. Orekhov, F. Ortica, M. Pallavicini, L. Papp, L. Pelicci, Ö. Penek, L. Pietrofaccia, N. Pilipenko, A. Pocar, G. Raikov, M. T. Ranalli, G. Ranucci, A. Razeto, A. Re, M. Redchuk, N. Rossi, S. Schönert, D. Semenov, G. Settanta, M. Skorokhvatov, A. Singhal, O. Smirnov, A. Sotnikov, R. Tartaglia, G. Testera, E. Unzhakov, F. L. Villante, A. Vishneva, R. B. Vogelaar, F. von Feilitzsch, M. Wojcik, M. Wurm, S. Zavatarelli, K. Zuber, G. Zuzel, and Borexino Collaboration. Improved Measurement of Solar Neutrinos from the Carbon-Nitrogen-Oxygen Cycle by Borexino and Its Implications for the Standard Solar Model. *Phys. Rev. Lett.*, 129 (25):252701, Dec. 2022. doi: 10.1103/PhysRevLett.129.252701.

M. Asplund, N. Grevesse, and A. J. Sauval. The Solar Chemical Composition. In I. Barnes, Thomas G. and F. N. Bash, editors, *Cosmic Abundances as Records of Stellar Evolution and Nucleosynthesis*, volume 336 of *Astronomical Society of the Pacific Conference Series*, page 25, Sept. 2005.

M. Asplund, N. Grevesse, A. J. Sauval, and P. Scott. The Chemical Composition of the Sun. *Annu. Rev. Astron. Astrophys.*, 47(1):481–522, Sept. 2009. doi: 10.1146/annurev.astro.46.060407.145222.

M. Asplund, A. M. Amarsi, and N. Grevesse. The chemical make-up of the Sun: A 2020 vision. *Astron. Astrophys.*, 653:A141, Sept. 2021. doi: 10.1051/0004-6361/202140445.

J. N. Bahcall. *Neutrino astrophysics / John N. Bahcall*. Cambridge University Press Cambridge [England] ; New York, 1989. ISBN 0521351138 052137975. URL `http://www.loc.gov/catdir/toc/cam021/88039165.html`.

J. N. Bahcall, M. H. Pinsonneault, and G. J. Wasserburg. Solar models with helium and heavy-element diffusion. *Reviews of Modern Physics*, 67(4):781–808, Oct. 1995. doi: 10.1103/RevModPhys.67.781.

J. E. Bailey, T. Nagayama, G. P. Loisel, G. A. Rochau, C. Blancard, J. Colgan, P. Cosse, G. Faussurier, C. J. Fontes, F. Gilleron, I. Golovkin, S. B. Hansen, C. A. Iglesias, D. P. Kilcrease, J. J. Macfarlane, R. C. Mancini, S. N. Nahar, C. Orban, J. C. Pain, A. K. Pradhan, M. Sherrill, and B. G. Wilson. A higher-than-predicted measurement of iron opacity at solar interior temperatures. *Nature*, 517(7532):56–59, Jan. 2015. doi: 10.1038/nature14048.

S. Basu. Global seismology of the Sun. *Living Reviews in Solar Physics*, 13(1):2, Aug. 2016. doi: 10.1007/s41116-016-0003-4.

S. Basu and H. M. Antia. Seismic measurement of the depth of the solar convection zone. *Mon. Not. R. Astron. Soc.*, 287(1):189–198, May 1997. doi: 10.1093/mnras/287.1.189.

S. Basu and H. M. Antia. Constraining Solar Abundances Using Helioseismology. *Astrophys. J. Lett.*, 606(1):L85–L88, May 2004. doi: 10.1086/421110.

S. Basu, H. M. Antia, and D. Narasimha. Helioseismic measurement of the extent of overshoot below the solar convection zone. *Mon. Not. R. Astron. Soc.*, 267:209, Mar. 1994. doi: 10.1093/mnras/267.1.209.

S. Basu, M. H. Pinsonneault, and J. N. Bahcall. How Much Do Helioseismological Inferences Depend on the Assumed Reference Model? *Astrophys. J.*, 529(2):1084–1100, Feb. 2000. doi: 10.1086/308302.

S. Basu, W. J. Chaplin, Y. Elsworth, R. New, and A. M. Serenelli. Fresh Insights on the Structure of the Solar Core. *Astrophys. J.*, 699(2):1403–1417, July 2009. doi: 10.1088/0004-637X/699/2/1403.

J. G. Beck. A comparison of differential rotation measurements - (Invited Review). *Sol. Phys.*, 191(1):47–70, Jan. 2000. doi: 10.1023/A:1005226402796.

J. Bergström, M. C. Gonzalez-Garcia, M. Maltoni, C. Peña-Garay, A. M. Serenelli, and N. Song. Updated determination of the solar neutrino fluxes from solar neutrino data. *Journal of High Energy Physics*, 2016:132, Mar. 2016. doi: 10.1007/JHEP03(2016)132.

E. Böhm-Vitense. Über die Wasserstoffkonvektionszone in Sternen verschiedener Effektivtemperaturen und Leuchtkräfte. Mit 5 Textabbildungen. *Zeitschrift für Astrophysik*, 46:108, Jan. 1958.

Borexino Collaboration, M. Agostini, K. Altenmüller, S. Appel, V. Atroshchenko, Z. Bagdasarian, D. Basilico, G. Bellini, J. Benziger, D. Bick, G. Bonfini, D. Bravo, B. Caccianiga, F. Calaprice, A. Caminata, S. Caprioli, M. Carlini, P. Cavalcante, A. Chepurnov, K. Choi, L. Collica, D. D'Angelo, S. Davini, A. Derbin, X. F. Ding, A. Di Ludovico, L. Di Noto, I. Drachnev, K. Fomenko, A. Formozov, D. Franco, F. Gabriele, C. Galbiati, C. Ghiano, M. Giammarchi, A. Goretti, M. Gromov, D. Guffanti, C. Hagner, T. Houdy, E. Hungerford, A. Ianni, A. Ianni, A. Jany, D. Jeschke, V. Kobychev, D. Korablev, G. Korga, D. Kryn, M. Laubenstein, E. Litvinovich, F. Lombardi, P. Lombardi, L. Ludhova, G. Lukyanchenko, L. Lukyanchenko, I. Machulin, G. Manuzio, S. Marcocci, J. Martyn, E. Meroni, M. Meyer, L. Miramonti, M. Misiaszek, V. Muratova, B. Neumair, L. Oberauer, B. Opitz, V. Orekhov, F. Ortica, M. Pallavicini, L. Papp,

Ö. Penek, N. Pilipenko, A. Pocar, A. Porcelli, G. Raikov, G. Ranucci, A. Razeto, A. Re, M. Redchuk, A. Romani, R. Roncin, N. Rossi, S. Schönert, D. Semenov, M. Skorokhvatov, O. Smirnov, A. Sotnikov, L. F. F. Stokes, Y. Suvorov, R. Tartaglia, G. Testera, J. Thurn, M. Toropova, E. Unzhakov, F. L. Villante, A. Vishneva, R. B. Vogelaar, F. von Feilitzsch, H. ang, S. Weinz, M. Wojcik, M. Wurm, Z. Yokley, O. Zaimidoroga, S. Zavatarelli, K. Zuber, and G. Zuzel. Comprehensive measurement of pp-chain solar neutrinos. *Nature*, 562(7728):505–510, Oct. 2018. doi: 10.1038/s41586-018-0624-y.

A. Bressan, P. Marigo, L. Girardi, B. Salasnich, C. Dal Cero, S. Rubele, and A. Nanni. PARSEC: stellar tracks and isochrones with the PAdova and TRieste Stellar Evolution Code. *Mon. Not. R. Astron. Soc.*, 427(1):127–145, Nov. 2012. doi: 10.1111/j.1365-2966.2012.21948.x.

A. G. Bressan, C. Chiosi, and G. Bertelli. Mass loss and overshooting in massive stars. *Astron. Astrophys.*, 102(1):25–30, Sept. 1981.

E. Caffau, H. G. Ludwig, M. Steffen, B. Freytag, and P. Bonifacio. Solar Chemical Abundances Determined with a CO5BOLD 3D Model Atmosphere. *Sol. Phys.*, 268(2):255–269, Feb. 2011. doi: 10.1007/s11207-010-9541-4.

S. Chandrasekhar. A General Variational Principle Governing the Radial and the Non-Radial Oscillations of Gaseous Masses. *Astrophys. J.*, 139:664, Feb. 1964. doi: 10.1086/147792.

J. Christensen-Dalsgaard. Helioseismology. *Reviews of Modern Physics*, 74(4):1073–1129, nov 2002. doi: 10.1103/revmodphys.74.1073. URL `https://doi.org/10.1103%2Frevmodphys.74.1073`.

J. Christensen-Dalsgaard, M. J. P. F. G. Monteiro, and M. J. Thompson. Helioseismic estimation of convective overshoot in the Sun. *Mon. Not. R. Astron. Soc.*, 276:283–292, Sept. 1995. doi: 10.1093/mnras/276.1.283.

J. Christensen-Dalsgaard, M. P. di Mauro, G. Houdek, and F. Pijpers. On the opacity change required to compensate for the revised solar composition. *Astron. Astrophys.*, 494(1):205–208, Jan. 2009. doi: 10.1051/0004-6361:200810170.

J. Christensen-Dalsgaard, M. J. P. F. G. Monteiro, M. Rempel, and M. J. Thompson. A more realistic representation of overshoot at the base of the solar convective envelope as seen by helioseismology. *Mon. Not. R. Astron. Soc.*, 414(2):1158–1174, June 2011. doi: 10.1111/j.1365-2966.2011.18460.x.

J. Colgan, D. P. Kilcrease, N. H. Magee, M. E. Sherrill, J. Abdallah, J., P. Hakel, C. J. Fontes, J. A. Guzik, and K. A. Mussack. A New Generation of Los Alamos Opacity Tables. *Astrophys. J.*, 817(2):116, Feb. 2016. doi: 10.3847/0004-637X/817/2/116.

R. H. Cyburt, A. M. Amthor, R. Ferguson, Z. Meisel, K. Smith, S. Warren, A. Heger, R. D. Hoffman, T. Rauscher, A. Sakharuk, H. Schatz, F. K. Thielemann, and M. Wiescher. The JINA REACLIB Database: Its Recent Updates and Impact on Type-I X-ray Bursts. *Astrophys. J. Suppl. Ser.*, 189(1):240–252, July 2010. doi: 10.1088/0067-0049/189/1/240.

D. Foreman-Mackey, D. W. Hogg, D. Lang, and J. Goodman. emcee: The MCMC hammer. *Publications of the Astronomical Society of the Pacific*, 125(925):306–312, mar 2013. doi: 10.1086/670067. URL `https://doi.org/10.1086%2F670067`.

J. Goodman and J. Weare. Ensemble samplers with affine invariance. *Communications in Applied Mathematics and Computational Science*, 5(1):65–80, Jan. 2010. doi: 10.2140/camcos.2010.5.65.

N. Grevesse and A. J. Sauval. Standard Solar Composition. *Space Sci. Rev.*, 85:161–174, May 1998. doi: 10.1023/A:1005161325181.

D. B. Guenther. Age of the Sun. *Astrophys. J.*, 339:1156, Apr. 1989. doi: 10.1086/167370.

D. B. Guenther, P. Demarque, Y. C. Kim, and M. H. Pinsonneault. Standard Solar Model. *Astrophys. J.*, 387:372, Mar. 1992. doi: 10.1086/171090.

J. A. Guzik and K. Mussack. Exploring Mass Loss, Low-Z Accretion, and Convective Overshoot in Solar Models to Mitigate the Solar Abundance Problem. *Astrophys. J.*, 713(2):1108–1119, Apr. 2010. doi: 10.1088/0004-637X/713/2/1108.

P. Hakel and D. P. Kilcrease. CHEMEOS: A New Chemical-Picture-Based Model for Plasma Equation-of-State Calculations. In J. S. Cohen, D. P. Kilcrease, and S. Mazavet, editors, *Atomic Processes in Plasmas: 14th APS Topical Conference on Atomic Processes in Plasmas*, volume 730 of *American Institute of Physics Conference Series*, pages 190–199, Oct. 2004. doi: 10.1063/1.1824870.

D. G. Hummer and D. Mihalas. The Equation of State for Stellar Envelopes. I. an Occupation Probability Formalism for the Truncation of Internal Partition Functions. *Astrophys. J.*, 331:794, Aug. 1988. doi: 10.1086/166600.

C. A. Iglesias and F. J. Rogers. Updated Opal Opacities. *Astrophys. J.*, 464:943, June 1996. doi: 10.1086/177381.

M. Joyce and J. Tayar. A Review of the Mixing Length Theory of Convection in 1D Stellar Modeling. *arXiv e-prints*, art. arXiv:2303.09596, Mar. 2023. doi: 10.48550/arXiv.2303.09596.

D. P. Kilcrease, J. Colgan, P. Hakel, C. J. Fontes, and M. E. Sherrill. Equations of State for Opacity Calculations. In *Workshop on Astrophysical Opacities*, volume 515 of *Astronomical Society of the Pacific Conference Series*, page 23, Aug. 2018.

K. Lodders, H. Palme, and H. P. Gail. Abundances of the Elements in the Solar System. *Landolt Börnstein*, 4B:712, Jan. 2009. doi: 10.1007/978-3-540-88055-4_34.

E. Magg, M. Bergemann, A. Serenelli, M. Bautista, B. Plez, U. Heiter, J. M. Gerber, H.-G. Ludwig, S. Basu, J. W. Ferguson, H. C. Gallego, S. Gamrath, P. Palmeri, and P. Quinet. Observational constraints on the origin of the elements. IV. Standard composition of the Sun. *Astron. Astrophys.*, 661:A140, May 2022. doi: 10.1051/0004-6361/202142971.

P. Marigo and B. Aringer. Low-temperature gas opacity. ÆSOPUS: a versatile and quick computational tool. *Astron. Astrophys.*, 508(3):1539–1569, Dec. 2009. doi: 10.1051/0004-6361/200912598.

P. Marigo, B. Aringer, L. Girardi, and A. Bressan. Updated Low-temperature Gas Opacities with ÆSOPUS 2.0. *Astrophys. J.*, 940(2):129, Dec. 2022. doi: 10.3847/1538-4357/ac9b40.

J. Montalbán, A. Miglio, A. Noels, N. Grevesse, and M. P. di Mauro. Solar Model with CNO Revised Abundances. In D. Danesy, editor, *SOHO 14 Helio- and Asteroseismology: Towards a Golden Future*, volume 559 of *ESA Special Publication*, page 574, Oct. 2004. doi: 10.48550/arXiv.astro-ph/0408055.

C. R. Proffitt and G. Michaud. Diffusion and Mixing of Lithium and Helium in Population II Dwarfs. *Astrophys. J.*, 371:584, Apr. 1991. doi: 10.1086/169923.

C. J. Schrijver and C. Zwaan. *Solar and Stellar Magnetic Activity*. Cambridge Astrophysics. Cambridge University Press, 2000. doi: 10.1017/CBO9780511546037.

A. Serenelli. Alive and well: A short review about standard solar models. *European Physical Journal A*, 52(4):78, Apr. 2016. doi: 10.1140/epja/i2016-16078-1.

A. M. Serenelli, S. Basu, J. W. Ferguson, and M. Asplund. New Solar Composition: The Problem with Solar Models Revisited. *Astrophys. J. Lett.*, 705(2):L123–L127, Nov. 2009. doi: 10.1088/0004-637X/705/2/L123.

A. M. Serenelli, W. C. Haxton, and C. Peña-Garay. Solar Models with Accretion. I. Application to the Solar Abundance Problem. *Astrophys. J.*, 743(1):24, Dec. 2011. doi: 10.1088/0004-637X/743/1/24.

G. Shaviv and E. E. Salpeter. Convective Overshooting in Stellar Interior Models. *Astrophys. J.*, 184:191–200, Aug. 1973. doi: 10.1086/152318.

D. Vescovi, L. Piersanti, S. Cristallo, M. Busso, F. Vissani, S. Palmerini, S. Simonucci, and S. Taioli. Effects of a revised ^{7}Be e^{-}-capture rate on solar neutrino fluxes. *Astron. Astrophys.*, 623:A126, Mar. 2019. doi: 10.1051/0004-6361/201834993.

F. L. Villante. Constraints on the Opacity Profile of the Sun from Helioseismic Observables and Solar Neutrino Flux Measurements. *Astrophys. J.*, 724(1):98–110, Nov. 2010. doi: 10.1088/0004-637X/724/1/98.

F. L. Villante, A. M. Serenelli, F. Delahaye, and M. H. Pinsonneault. The Chemical Composition of the Sun from Helioseismic and Solar Neutrino Data. *Astrophys. J.*, 787(1):13, May 2014. doi: 10.1088/0004-637X/787/1/13.

N. Vinyoles, A. M. Serenelli, F. L. Villante, S. Basu, J. Bergström, M. C. Gonzalez-Garcia, M. Maltoni, C. Peña-Garay, and N. Song. A New Generation of Standard Solar Models. *Astrophys. J.*, 835(2):202, Feb. 2017. doi: 10.3847/1538-4357/835/2/202.

R. C. Willson and H. S. Hudson. The Sun's luminosity over a complete solar cycle. *Nature*, 351(6321):42–44, May 1991. doi: 10.1038/351042a0.

Appendix A

FEn MCMC plots

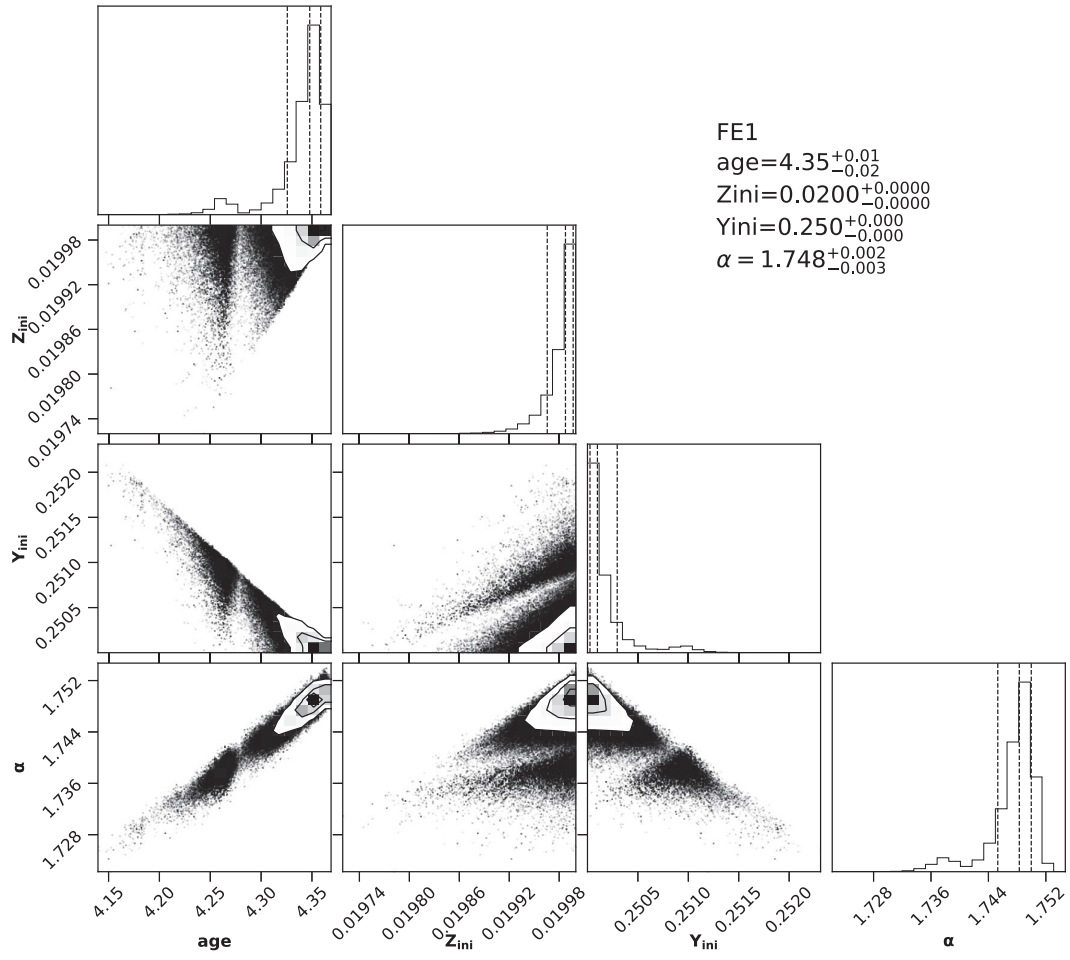

Figure A.1. Posterior distributions for the four parameters $(\text{age}, Z_{\text{ini}}, Y_{\text{ini}}, \alpha)$ with their best estimates for model FE1.

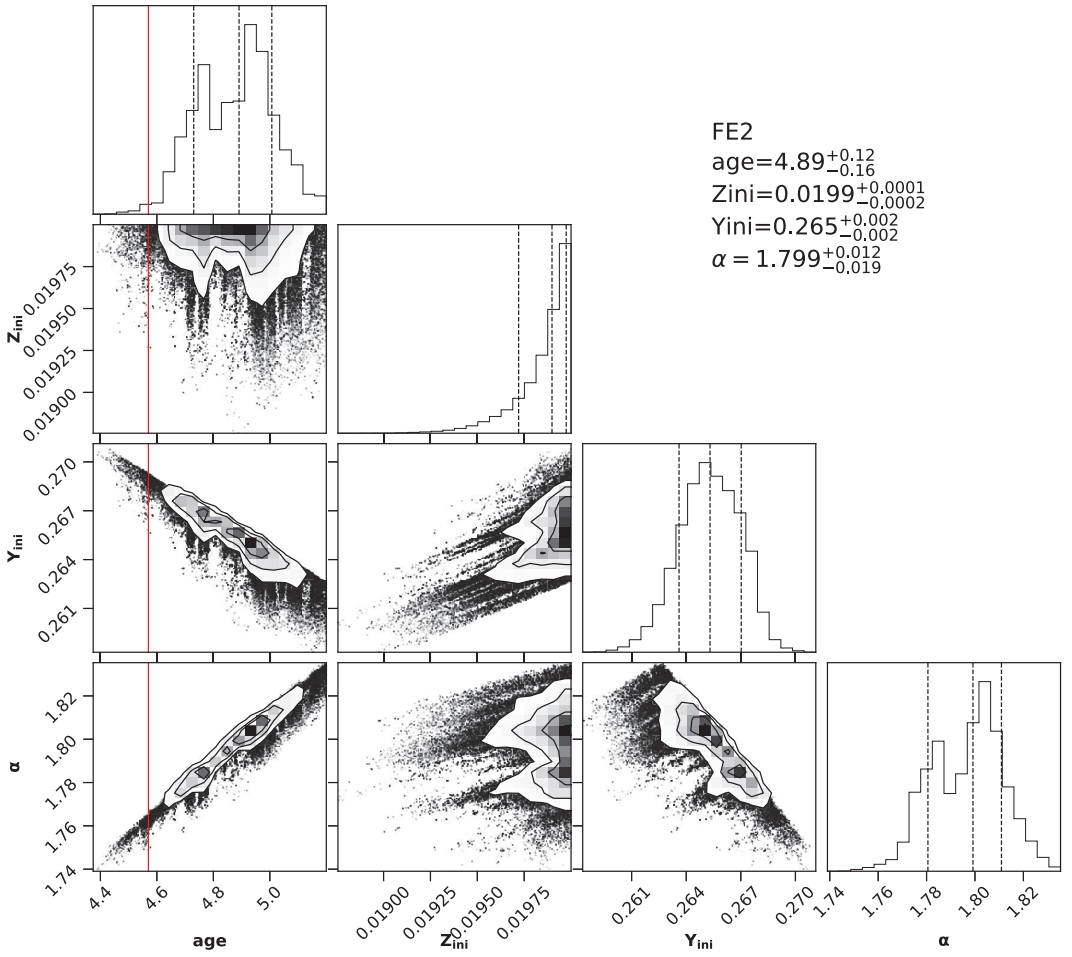

Figure A.2. Posterior distributions for the four parameters $(\text{age}, Z_{\text{ini}}, Y_{\text{ini}}, \alpha)$ with their best estimates for model FE2. The red line represents the reference value for the age of the Sun $t_{\odot}$.

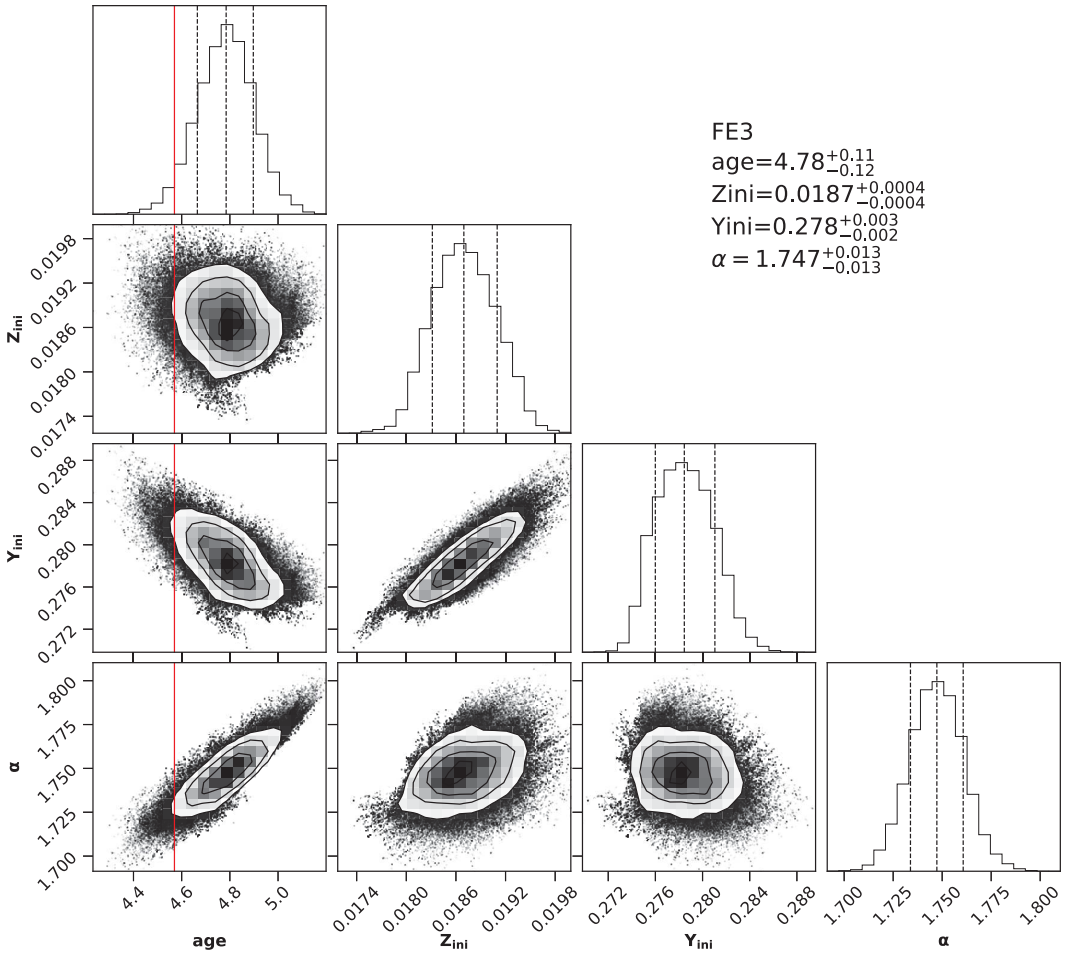

Figure A.3. Posterior distributions for the four parameters $(\text{age}, Z_{\text{ini}}, Y_{\text{ini}}, \alpha)$ with their best estimates for model FE3. The red line represents the reference value for the age of the Sun $t_{\odot}$.

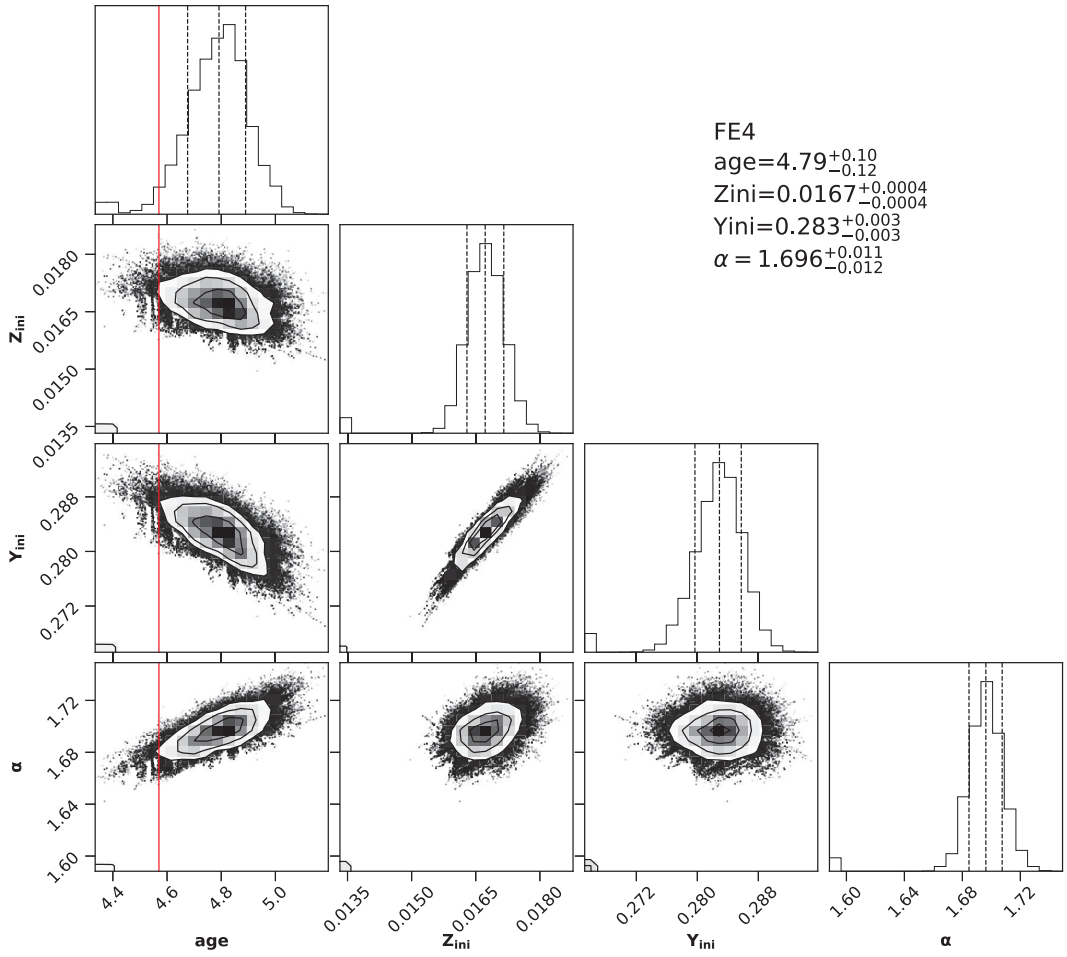

Figure A.4. Posterior distributions for the four parameters $(\text{age}, Z_{\text{ini}}, Y_{\text{ini}}, \alpha)$ with their best estimates for model FE4. The red line represents the reference value for the age of the Sun $t_{\odot}$.

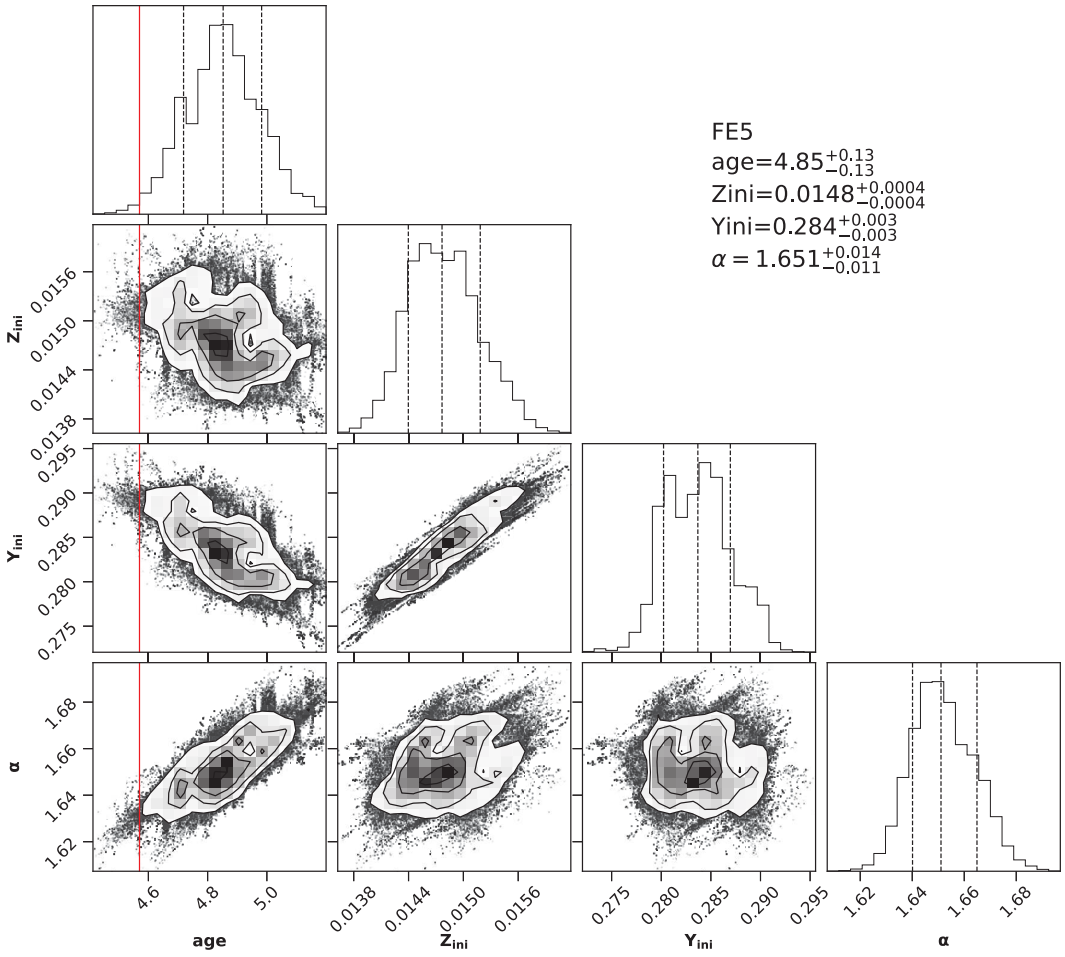

Figure A.5. Posterior distributions for the four parameters $(\text{age}, Z_{\text{ini}}, Y_{\text{ini}}, \alpha)$ with their best estimates for model FE5. The red line represents the reference value for the age of the Sun $t_{\odot}$.

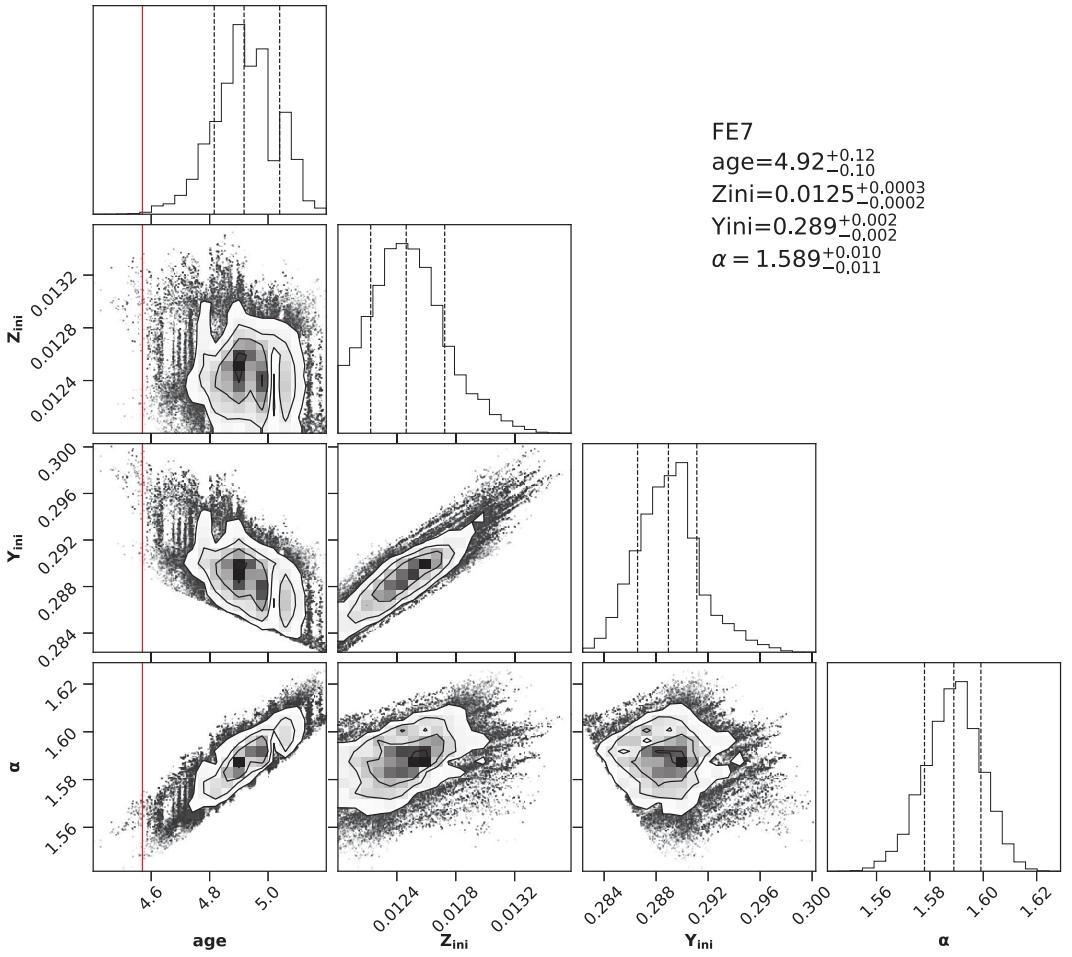

Figure A.6. Posterior distributions for the four parameters $(\text{age}, Z_{\text{ini}}, Y_{\text{ini}}, \alpha)$ with their best estimates for model FE7. The red line represents the reference value for the age of the Sun $t_{\odot}$.

Appendix B

Overshooting MCMC plots

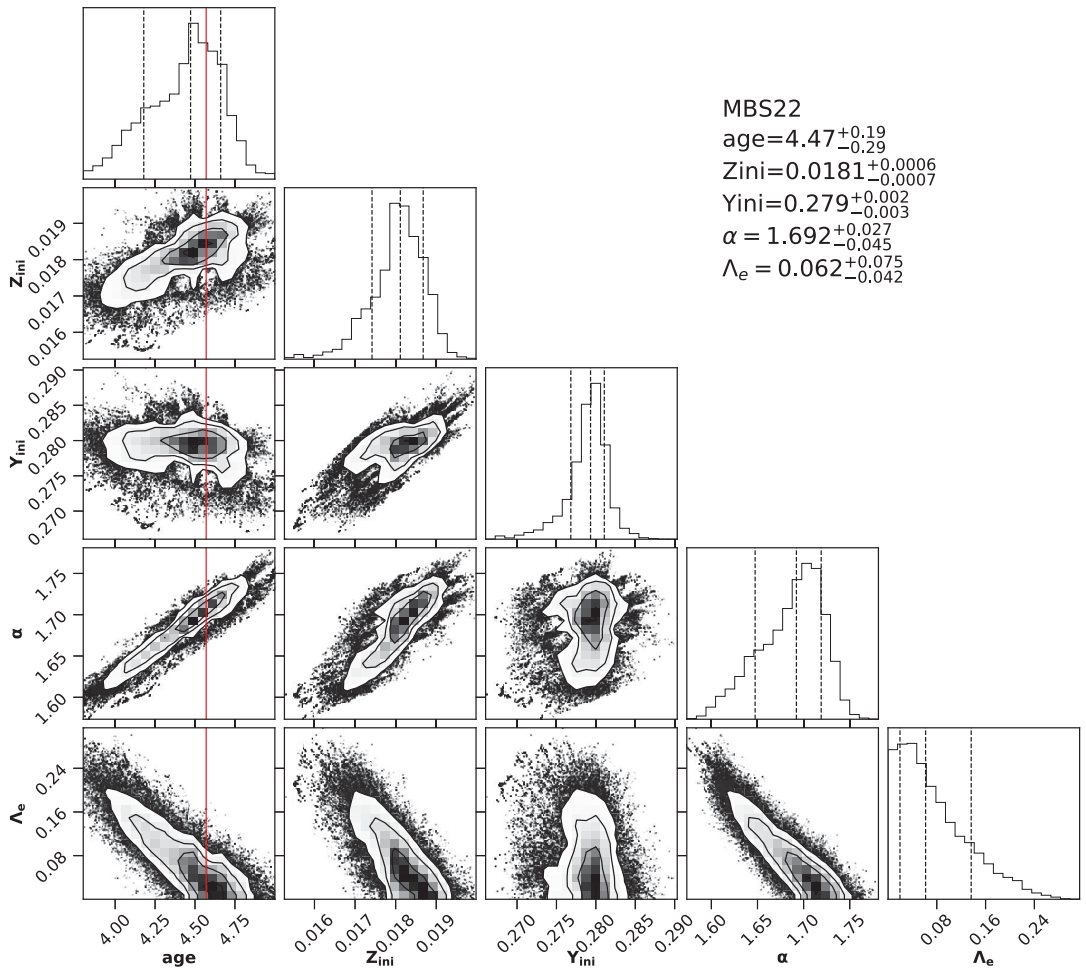

Figure B.1. Posterior distributions for the five parameters $(\text{age}, Z_{\text{ini}}, Y_{\text{ini}}, \alpha, \Lambda_e)$ with their best estimates for model MBS22.

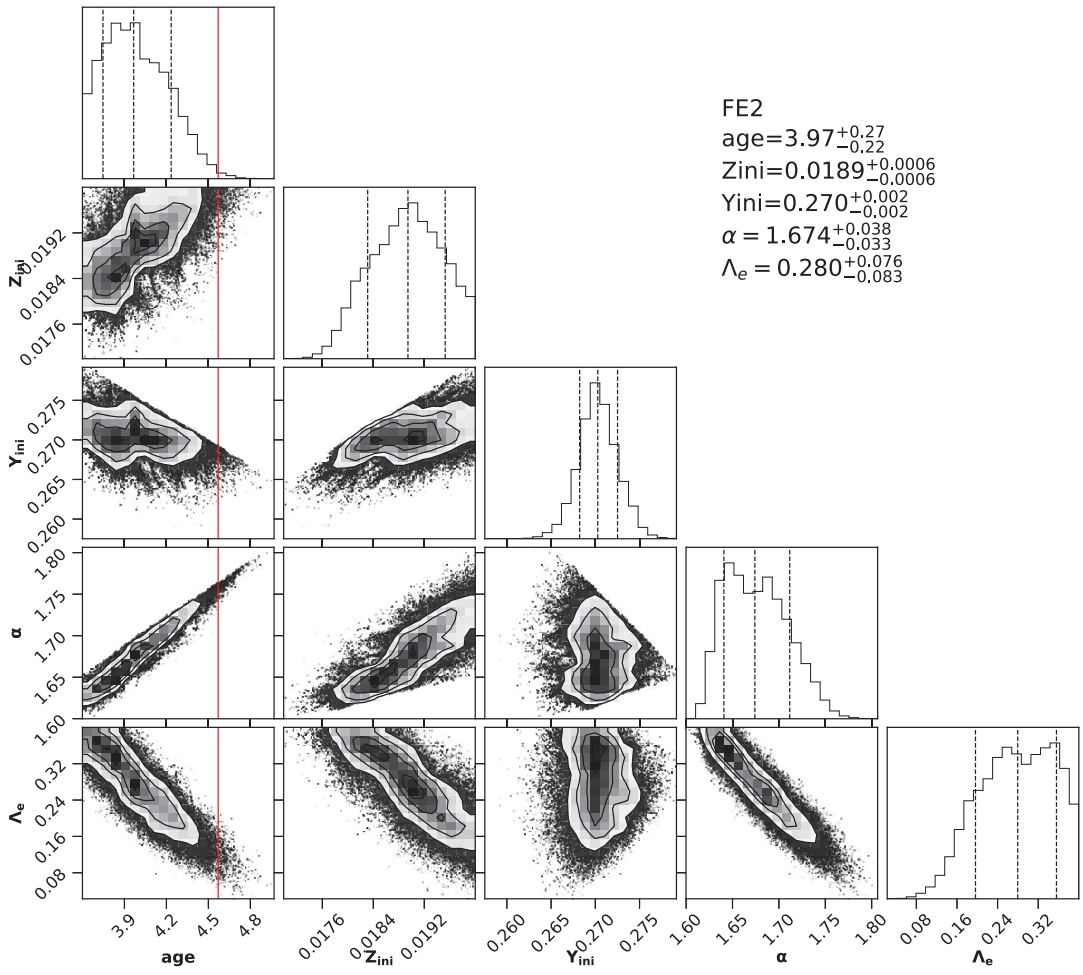

Figure B.2. Posterior distributions for the five parameters $(\text{age}, Z_{\text{ini}}, Y_{\text{ini}}, \alpha, \Lambda_e)$ with their best estimates for model FE2.

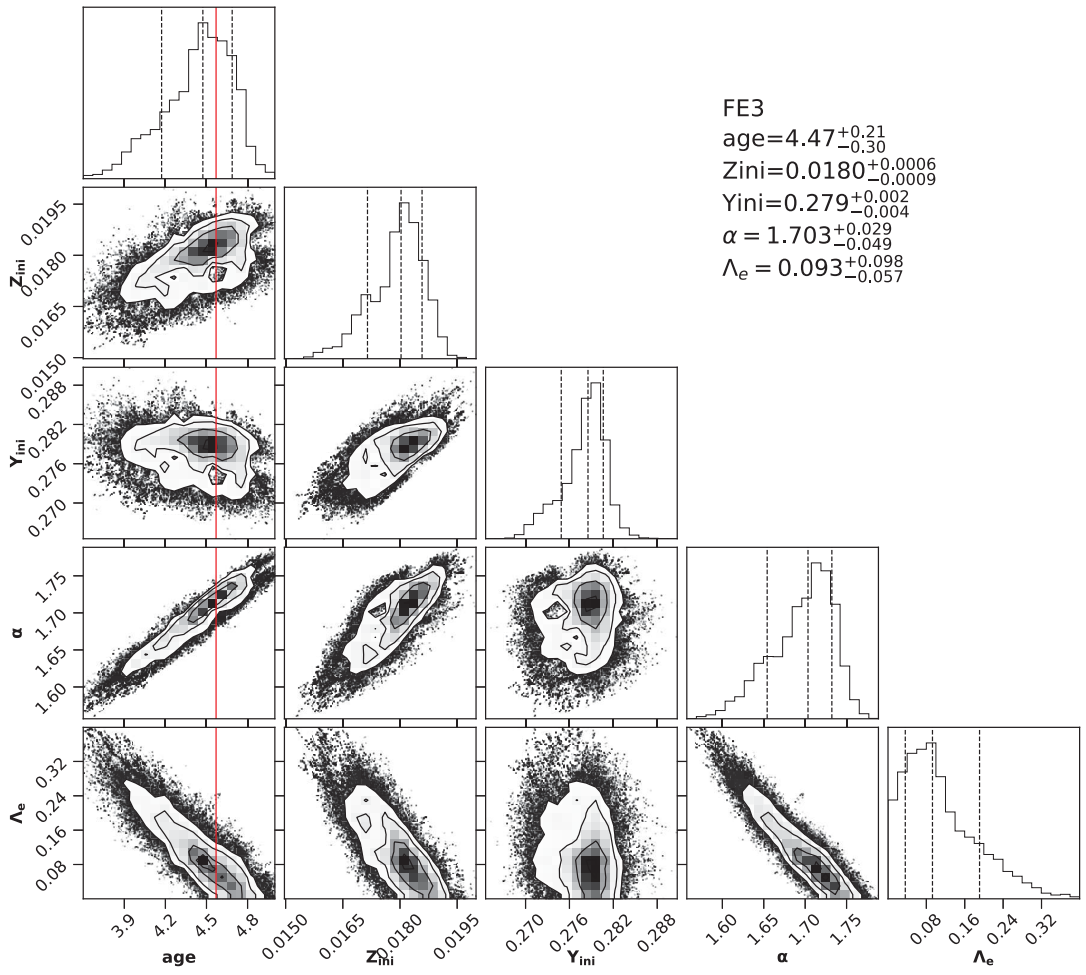

Figure B.3. Posterior distributions for the five parameters $(\text{age}, Z_{\text{ini}}, Y_{\text{ini}}, \alpha, \Lambda_e)$ with their best estimates for model FE3.

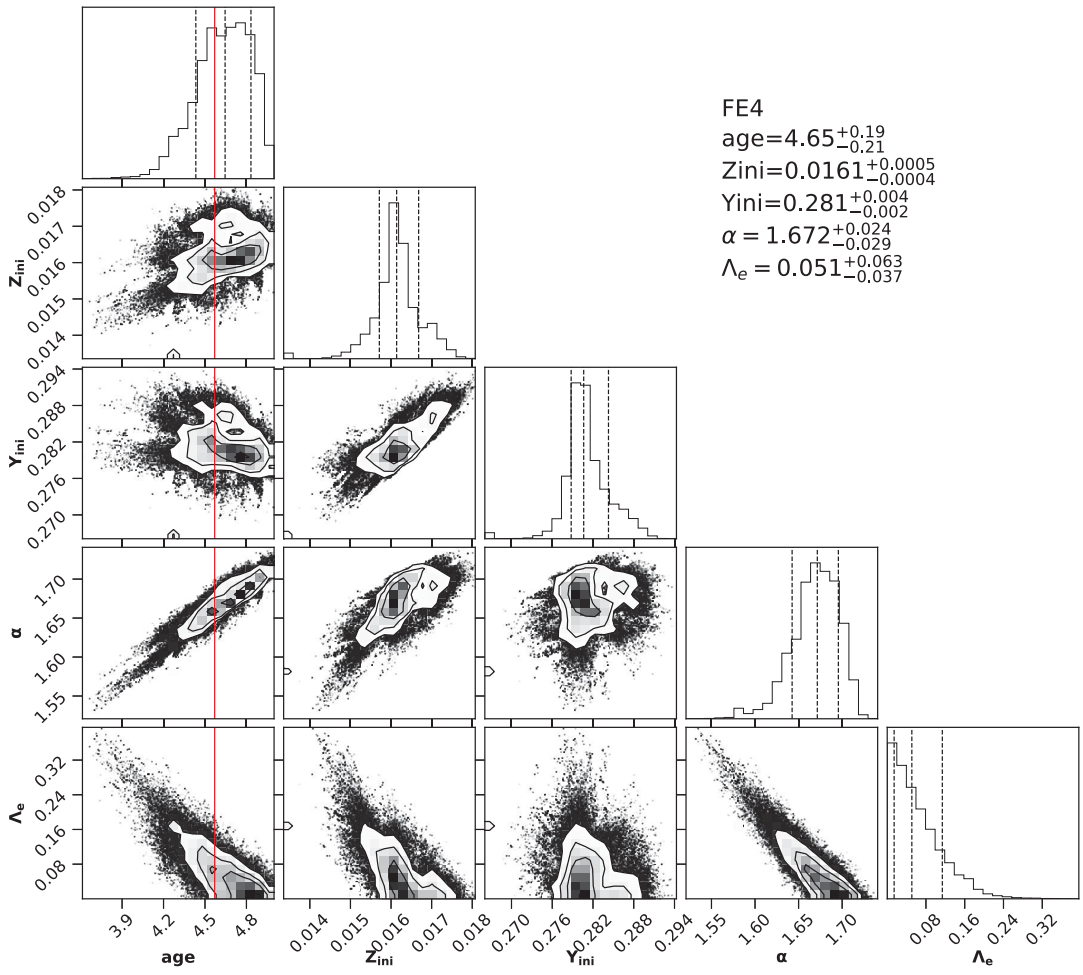

Figure B.4. Posterior distributions for the five parameters $(\text{age}, Z_{\text{ini}}, Y_{\text{ini}}, \alpha, \Lambda_e)$ with their best estimates for model FE4.

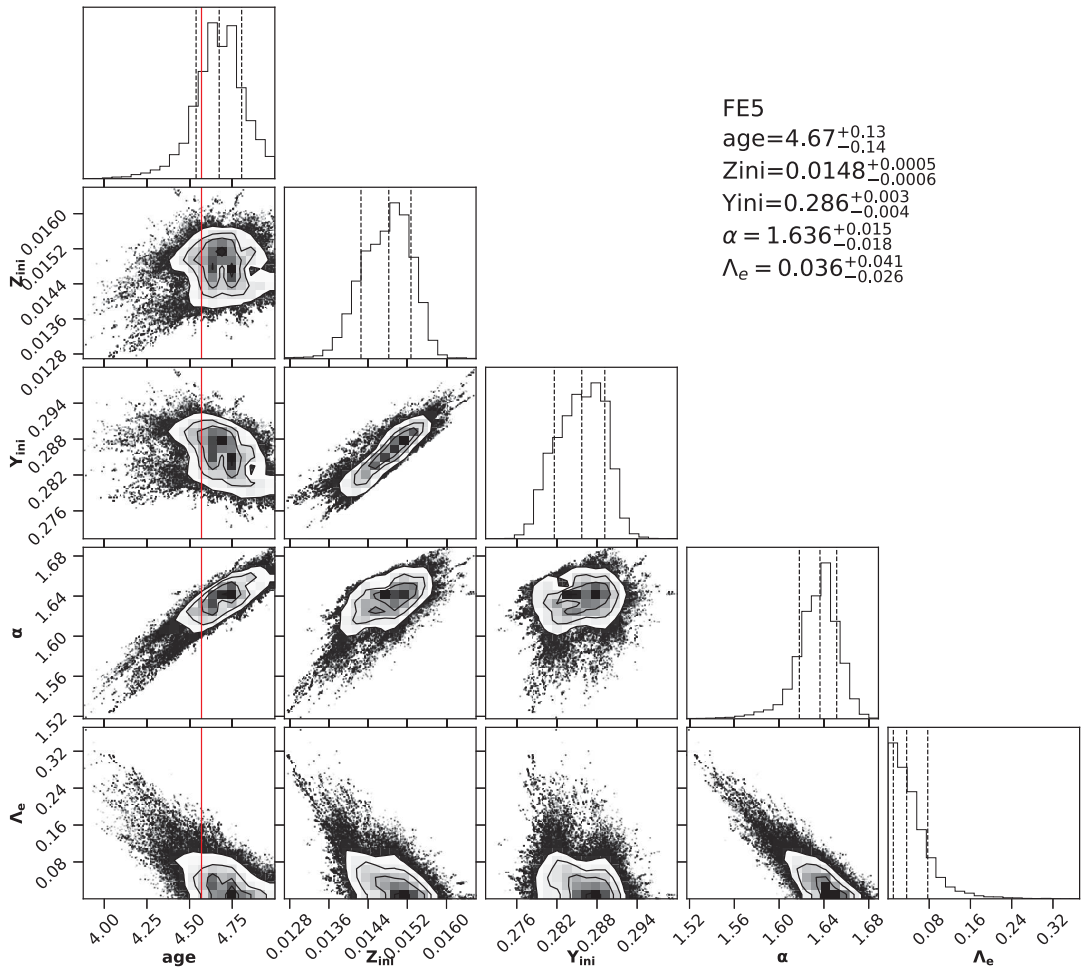

Figure B.5. Posterior distributions for the five parameters $(\text{age}, Z_{\text{ini}}, Y_{\text{ini}}, \alpha, \Lambda_e)$ with their best estimates for model FE5.

Appendix C

Differential neutrino flux

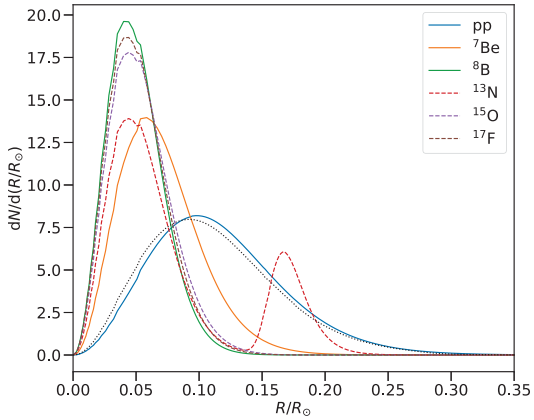

Figure C.1. MBS22

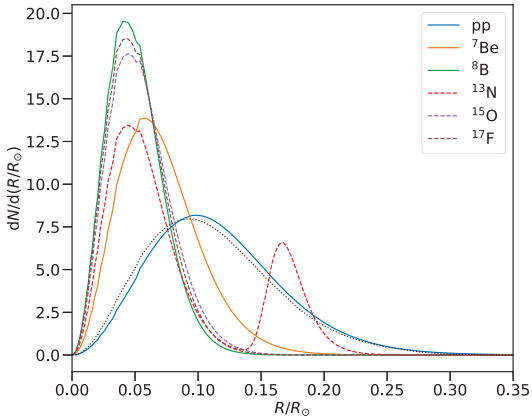

Figure C.2. MBS22-ovr

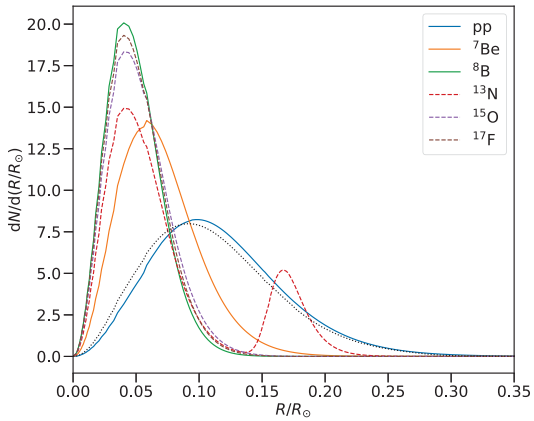

Figure C.3. FE3

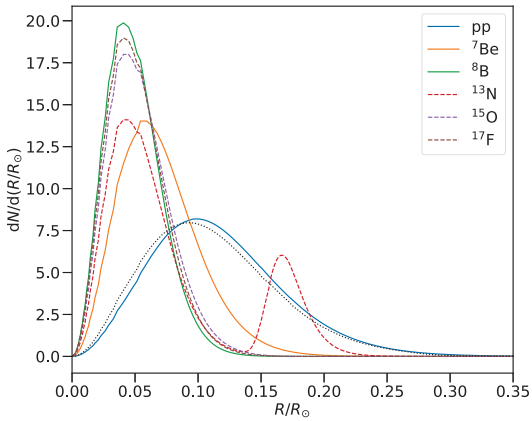

Figure C.4. FE3-ovr

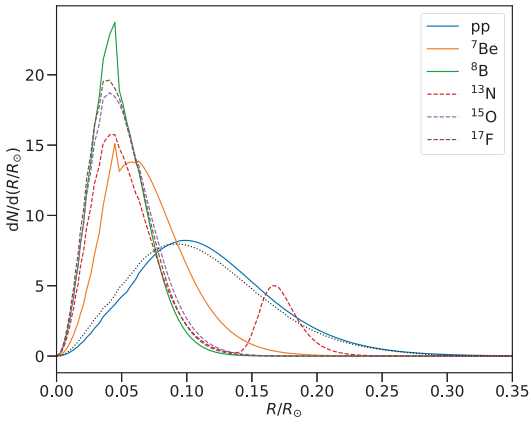

Figure C.5. FE4

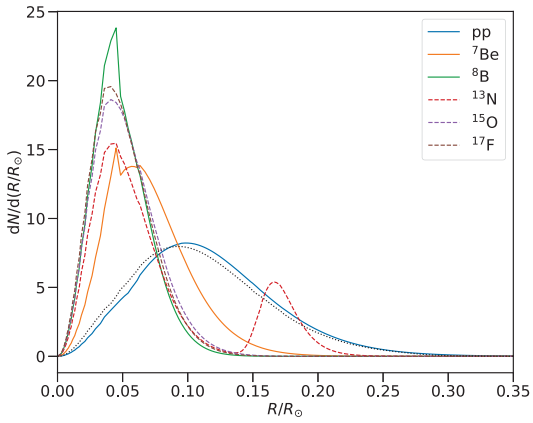

Figure C.6. FE4-ovr

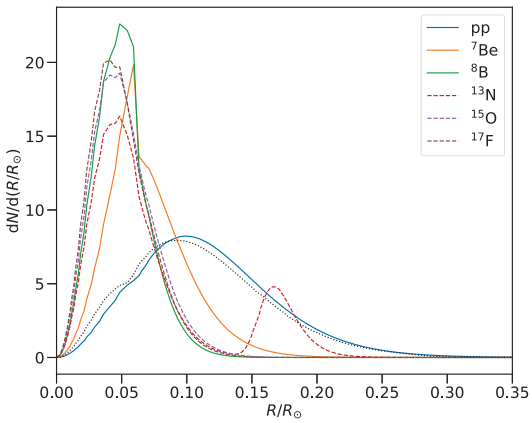

Figure C.7. FE5

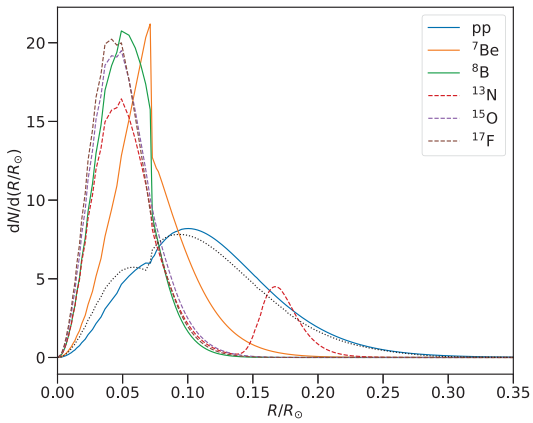

Figure C.8. FE7

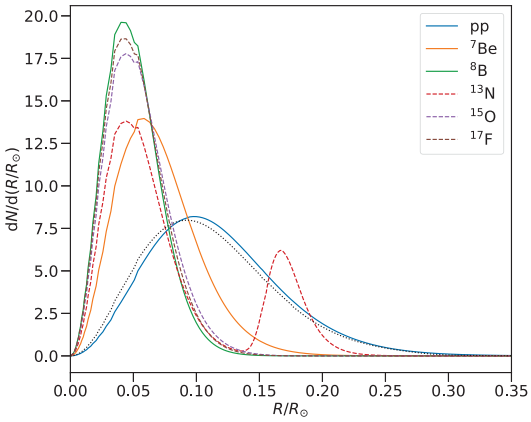

Figure C.9. C11

Ringraziamenti

Dopo cinque intensi anni trascorsi nell'ambiente accademico, vorrei esprimere la mia gratitudine a tutte le persone che hanno reso possibile il raggiungimento di questo grande traguardo.

Innanzitutto, desidero ringraziare la professoressa Marigo per la sua guida preziosa e il suo supporto costante, e per avermi proposto un progetto così stimolante e che mi permettesse di toccare con mano il mondo della ricerca. Un ringraziamento speciale va anche al professor Bressan, per il suo contributo prezioso e i suoi consigli illuminanti durante tutta la realizzazione del progetto. La sua competenza e il suo interesse per il mio lavoro hanno fatto la differenza. Voglio poi esprimere la mia riconoscenza al dott. Guglielmo Volpato, che mi ha seguito passo dopo passo nella mia ricerca, per la disponibilità, la gentilezza e la prontezza che ha sempre mostrato nell'aiutarmi. Un grazie va anche al dott. Alessandro Mazzi, per il preziosissimo aiuto con la stesura e l'ottimizzazione di alcuni pezzi di codice.

Il ringraziamento più grande va a mamma Mara, a papà Gianluca e a mia sorella Sofia, per il loro amore, il loro sostegno incondizionato e la loro costante fiducia in me, anche quando non condividevano a pieno le mie decisioni. Senza il vostro appoggio, tutto questo non sarebbe stato possibile.

A tutti i miei amici, che hanno condiviso gioie e sfide con me durante questi anni, voglio dire grazie per la vostra amicizia e il vostro incoraggiamento costante. In particolare ringrazio Davide, per il tempo dedicato ad ascoltarmi, i consigli, e le serate spensierate per staccare da tutto il resto. Un grande grazie va anche a Greta, per tutto il sostegno e il supporto durante questo ultimo periodo di università.

Infine, un ringraziamento speciale va a Maicol, per essermi sempre stato vicino, per la sua comprensione, per avermi sostenuto in ogni momento, per avermi sempre spronato a fare quello che fosse meglio per me nonostante le difficoltà. In questi anni non sono certo mancati i momenti difficili, e sono grato di averli potuti affrontare con te al mio fianco.

Questa tesi magistrale rappresenta non solo il mio impegno, ma anche il frutto della collaborazione e del supporto di tutte queste persone straordinarie. Grazie di cuore.